

1 **Title:**

2 Modeling dust as a component mineral in the Community Atmosphere Model: development of
3 framework and impact on radiative forcing.

5 **Authors:**

6 R. A. Scanza [ras486@cornell.edu]¹

7 N. Mahowald [mahowald@cornell.edu]¹

8 S. Ghan [steve.ghan@pnnl.gov]²

9 C. S. Zender [zender@uci.edu]³

10 J. F. Kok [jfkok@ucla.edu]^{1,4}

11 X. Liu [xliu6@uwyo.edu]^{2,5}

12 Y. Zhang [yan_zhang@fudan.edu.cn]^{1,6}

13 **Affiliations:**

14 1. Department of Earth and Atmospheric Sciences, Cornell University, Ithaca, New York, USA

15 2. Atmospheric Sciences and Global Change Division, Pacific Northwest National Laboratory,
16 Richland, Washington, USA

17 3. Department of Earth System Science, University of California, Irvine, USA

18 4. Department of Atmospheric and Oceanic Sciences, University of California, Los Angeles, USA

19 5. Department of Atmospheric Science, University of Wyoming, Laramie, Wyoming, USA

20 6. Department of Environmental Science and Engineering, Fudan University, Shanghai, China

22 **Abstract:**

23 The mineralogy of desert dust is important due to its effect on radiation, clouds and
24 biogeochemical cycling of trace nutrients. This study presents the simulation of dust radiative
25 forcing as a function of both mineral composition and size at the global scale using mineral soil
26 maps for estimating emissions. Externally mixed mineral aerosols in the bulk aerosol module in the
27 Community Atmosphere Model version 4 (CAM4) and internally mixed mineral aerosols in the
28 modal aerosol module in the Community Atmosphere Model version 5.1 (CAM5) embedded in the
29 Community Earth System Model version 1.0.5 (CESM) are speciated into common mineral
30 components in place of total dust. The simulations with mineralogy are compared to available
31 observations of mineral atmospheric distribution and deposition along with observations of clear-

ras486 11/17/14 3:13 PM

Deleted: Dependence of

ras486 11/17/14 3:13 PM

Deleted: radiative forcing on mineralogy

ras486 11/17/14 3:13 PM

Deleted: 2.

35 sky radiative forcing efficiency. Based on these simulations, we estimate the all-sky direct radiative
36 forcing at the top of the atmosphere as $+0.05 \text{ Wm}^{-2}$ for both CAM4 and CAM5 simulations with
37 mineralogy. We compare this ~~to the radiative forcing from~~ simulations of dust in release versions
38 of CAM4 and CAM5 ($+0.08$ and $+0.17 \text{ Wm}^{-2}$) and of dust with optimized optical properties, wet
39 scavenging and particle size distribution in CAM4 and CAM5, -0.05 and -0.17 Wm^{-2} , respectively.
40 The ability to correctly include the mineralogy of dust in climate models is hindered by its spatial
41 and temporal variability as well as insufficient global in-situ observations, incomplete and
42 uncertain source mineralogies and the uncertainties associated with data retrieved from remote
43 sensing methods.

44

45 1.0 Introduction:

46 Dust aerosols are soil particles suspended in the atmosphere, and they impact the climate
47 system by influencing the radiation budget, cloud processes (Miller and Tegen, 1998; Mahowald and
48 Kiehl, 2003; Karydis et al., 2011; DeMott et al., 2003; Levin et al., 2005), and various biogeochemical
49 cycles (Swap et al., 1992; Martin et al., 1991; Jickells et al., 2005). The radiation balance of the Earth
50 system is affected by the scattering and absorption of solar and infrared radiation by mineral
51 aerosols (Miller and Tegen, 1998; Sokolik and Toon, 1999). Both magnitude and sign of radiative
52 forcing of dust are considered to be one of the most uncertain aspects in determining the net
53 radiative forcing from natural and anthropogenic aerosols (IPCC, 2007).

54 Previous and ongoing modeling efforts address the importance of determining the mineral
55 composition of dust and its impact on the radiation budget (Sokolik and Toon, 1999; Claquin et al.,
56 1999; Balkanski et al., 2007). A main factor in accurately determining the sign of dust radiative
57 forcing is the inclusion of the mineralogical components that absorb solar radiation. For instance,
58 iron oxides have large imaginary portions of their complex refractive indices
59 (<http://www.atm.ox.ac.uk/project/RI/hematite.html>, cited as personal communication with
60 A.H.M.J. Triaud, 2005). Since the imaginary part of refractive indices corresponds to absorption,
61 iron oxide refractive indices control the amplitude of dust absorption in the solar and visible

ras486 11/17/14 3:13 PM

Deleted: and

ras486 11/17/14 3:13 PM

Deleted: both with

64 | wavelengths (Sokolik and Toon, 1999;Claquin et al., 1999;Moosmüller et al., 2012). Efforts to
65 | separate the components of absorbing dust single out the iron oxides, e.g., hematite and goethite,
66 | although in this study, we simulate the iron oxides collectively as hematite.

67 | Recent modeling studies that consider the speciation of dust into its mineral components
68 | include work by Balkanski et al., 2007, Sokolik and Toon, 1999, Nickovic et al., 2012, and Journet et
69 | al., 2014. Balkanski et al., 2007 reports good agreement with satellite and AERONET data (Holben
70 | et al., 1998;Holben et al., 2001) when a 1.5% internally mixed volume weighted percent of hematite
71 | is modeled, and reports global mean top of atmosphere (TOA) and surface radiative forcings
72 | between -0.47 to -0.24 Wm⁻² and -0.81 to -1.13 Wm⁻² respectively. Sokolik and Toon (1999)
73 | investigate the optical properties of a mixture of individual minerals and of mixtures where
74 | hematite is aggregated with other minerals. They find a net negative radiative forcing for externally
75 | mixed minerals and a net positive forcing when either hematite concentrations are unrealistically
76 | high or when hematite is aggregated with quartz. Nickovic et al. 2012 presents high resolution
77 | mineral maps based on Claquin et al. 1999 mineral maps. The maps include some improvements,
78 | for example, hematite is represented in both the clay and silt soil fractions, along with mapping
79 | additional soil types and including maps with phosphorus. Journet et al., 2014 expands on the soil
80 | mineralogies from Claquin et al., 1999 by including many additional soil mineralogy measurements
81 | and increasing the number of minerals; however, these maps were not available at the time the
82 | simulations in this study were performed.

83 | This study addresses the direct radiative forcing (DRF) of natural mineral aerosols in the
84 | Community Earth System Model, (CESM). The global model simulations attempt to match the sign
85 | and magnitude of regional observations of DRF using two different atmosphere models. Dust in the
86 | Community Atmosphere Model 4, hereafter CAM4, was speciated into eight minerals, illite,
87 | kaolinite, montmorillonite, hematite, quartz, calcite, gypsum and feldspar, (Claquin et al., 1999)
88 | where the minerals along with other aerosols are treated as external mixtures (Mahowald et al.,
89 | 2006). The Community Atmosphere Model 5, CAM5, treats aerosols as internal mixtures within
90 | two of three modes (Liu et al., 2012). Dust in CAM5 was speciated into four minerals, the major

ras486 11/17/14 3:13 PM

Deleted:

ras486 11/17/14 3:13 PM

Deleted: .

ras486 11/17/14 3:13 PM

Deleted: and

ras486 11/17/14 3:13 PM

Deleted: .

ras486 11/17/14 3:13 PM

Deleted: .

96 clays (illite, kaolinite and montmorillonite) and hematite, along with an additional tracer to carry
97 the rest of the dust.

98 The main objective of this work was to build the framework to model dust as its individual
99 mineral components and to test the accuracy of emission, advection and deposition of the mineral
100 tracers by comparing with observations from literature. An additional objective was to determine
101 the radiative effect of speciating dust into minerals on the Earth System. Furthermore, the use of
102 two different atmosphere models allows us to test the sensitivity of mineral speciation within
103 different frameworks. The framework for carrying extra tracers performs reasonably well and is
104 currently being used to investigate elemental distributions (Zhang et al., in prep) and also ice
105 nucleation in mixed-phase clouds as a function of different mineral species.

106 The sections are organized as follows: section 2 describes methods including a description
107 of the CESM and CAM4 and CAM5 methods for dust entrainment, transport and deposition as well
108 as the radiation schemes used to compute global estimates of DRF. Section 3 describes the
109 resulting mineral distributions and compares them with observations, compares modeled optical
110 depths and single scattering albedo to the Aerosol RObotic NETwork (AERONET) ground based sun
111 photometers (Holben et al., 1998; Holben et al., 2001), and provides global and regional estimates of
112 radiative forcing for both CAM4 and CAM5. Section 3 also presents two sensitivity studies, the first
113 on the dust size distribution to both illustrate the significance of including mineralogy and to
114 attempt to quantify the uncertainties associated with the radiative forcing from minerals. The
115 second sensitivity study involves simulating mineralogy with hematite solely in the soil clay map to
116 address recent studies that find hematite primarily in fine particle sizes and to investigate whether
117 or not this improves our estimates of radiative forcing. The last section discusses the strengths of
118 this framework and outlines where additional work is needed. Future improvements to these
119 models will be described along with planned future simulations of trace nutrient biogeochemical
120 cycling with this framework.

121

122 **2.0 Methods:**

ras486 11/18/14 11:10 AM

Deleted: . (Liu et al., in prep. 2013).

124 The Community Earth System Model version 1.0.5 (CESM 1.0.5), which is coordinated by the
125 National Center for Atmospheric Research (NCAR) is a coupled earth system model used to
126 simulate past, present and future climate (Hurrell et al., 2013). This study uses CESM1.0.5 with
127 modifications to CAM4 and CAM5.1 to simulate dust as distinct mineral tracers and to model
128 radiation online to investigate the DRF of mineralogy.

129

130 2.1 Desert dust model:

131 The CAM4 model configuration used for bulk aerosols contains active atmosphere, land and
132 sea ice components, as well as a data ocean and slab glacier forced by NASA's GEOS-5 meteorology
133 (FSDBAM) (Suarez et al., 2008;Hurrell et al., 2013;Lamarque et al., 2012). Model resolution is on a
134 $2.5^{\circ} \times 1.9^{\circ}$ horizontal grid with 56 vertical levels. The model was run for eight years, 2004-2011,
135 with the simulations from 2006 through 2011 used for analysis. The default configuration was
136 altered so that radiative feedbacks onto climate were active and the radiation code was modified to
137 compute radiation online, bypassing the need for Parallel Offline Radiative Transfer (PORT) (Conley
138 et al., 2013). Because we use reanalysis winds, radiation does not feed back onto the meteorology.
139 The dust model is part of a bulk aerosol model scheme with fixed bin width and sub-bin
140 distribution following the Dust Entrainment and Deposition Model (DEAD) (Zender et al., 2003).
141 The location and emission potential of dust source regions have been optimized from the default
142 configuration and are described in (Mahowald et al., 2006; [Albani et al., 2014](#)).

143 Measurements and theory show that dust aerosols ($0.1\text{-}50\mu\text{m}$) are primarily emitted
144 through saltation, the bouncing motion of sand-sized ($\sim 100\text{-}200\mu\text{m}$) particles [that disaggregate](#)
145 [and emit dust aerosols via sandblasting from the saltating particles](#) (Gillette et al., 1974;Shao et al.,
146 1993;Kok et al., 2012). In order for saltation to be initiated, the wind stress on the surface needs to
147 be sufficient to lift sand particles, which for bare soils, occurs above wind friction speeds of
148 approximately 0.2 ms^{-1} (Bagnold, 1941;Kok et al., 2012). Dust entrainment in the Community Land
149 Model (CLM), the land component of the CESM, is initiated after the wind speed exceeds the
150 threshold wind speed calculated by the model. The threshold wind speed for dust entrainment

ras486 11/17/14 3:13 PM

Deleted: ;Albani et al., submitted))

152 increases with soil moisture: CLM uses the semi-empirical relation of Fecan et al. (1999) with
 153 additional optimization from the traditional dependence of the square of clay mass fraction (Fecan
 154 et al., 1999;Zender et al., 2003). Regions of dust emission are parameterized as being associated
 155 with topographical depressions where sediment from hydrological systems accumulates (Ginoux et
 156 al., 2001;Yoshioka et al., 2007;Mahowald et al., 2006;Zender et al., 2003). While measurements of
 157 dust particle size distribution range from about 0.1-50 μm , the CESM only accounts for the
 158 climatologically most relevant portion (0.1-10 μm)(Schulz et al., 1998;Zender et al., 2003). Particle
 159 size distributions are computed from the mass fraction of an analytic trimodal lognormal
 160 probability density function representing three source modes to four discrete sink or transport bins
 161 by Equation 1 (Zender et al., 2003)

$$M_{i,j} = \frac{1}{2} \left[\text{erf} \left(\frac{\ln(D_{\max,j}/\overline{D_{v,j}})}{\sqrt{2} \ln(\sigma_{g,i})} \right) - \text{erf} \left(\frac{\ln(D_{\min,j}/\overline{D_{v,j}})}{\sqrt{2} \ln(\sigma_{g,i})} \right) \right], \quad (1)$$

162 where erf is the error function (Seinfeld and Pandis, 1998), D_{\max} and D_{\min} correspond to the
 163 transport bins bounded at diameters 0.1, 1.0, 2.5, 5.0 and 10.0 μm with a sub-bin lognormal
 164 distribution with mass median diameter, $\overline{D_v}$, of 3.5 μm and geometric standard deviation, $\sigma_g = 2$
 165 (Reid et al., 2003;Mahowald et al., 2006;Zender et al., 2003). The mass fraction in Equation 1 is 0.87
 166 for particle diameters $D=0.1-10 \mu\text{m}$ with the remaining fraction 0.13 centered around 19 μm . We
 167 assume this fraction is insignificant for long range transport (Zender et al., 2003). Particle size
 168 distributions were parameterized (default mass fractions are 3.8, 11.1,17.2 and 67.8% for size bins
 169 1-4) following the brittle fragmentation theory of dust emission (Kok, 2011), with prescribed mass
 170 fractions in each bin of 1.1, 8.7, 27.7 and 62.5% respectively. The parameterized size distribution
 171 resulted in better agreement with AERONET size distribution measurements (Albani et al., 2014)
 172 Dry deposition includes gravitational settling and turbulent deposition and wet deposition includes
 173 in-cloud nucleation scavenging and below-cloud scavenging (Rasch et al., 2000;Zender et al.,
 174 2003;Mahowald et al., 2006). The scavenging coefficients and particle solubility parameterizations
 175 were modified from (0.1, 0.1 for bins 3 and 4) to (0.3, 0.3 for bins 3 and 4), and the prescribed
 176 solubility was changed from 0.15 to 0.3 (Albani et al., 2014). The suppression of dust emission by

177 vegetation (Lancaster and Baas, 1998;Okin, 2008) was parameterized by assuming that the fraction
178 of the grid cell consisting of bare soil capable of emitting dust aerosols decreases linearly with the
179 leaf area index up to a threshold of 0.3 m²/m² (Mahowald et al., 2006).

180 The CAM5 model configuration used for modal aerosols is stand-alone atmosphere with
181 land and sea ice components, as well as a data ocean and slab glacier, forced by NASA's GEOS-5
182 meteorology (Suarez et al., 2008;Lamarque et al., 2012;[Hurrell et al., 2013](#)) and CAM5 physics
183 (FC5)(Liu et al., 2012). Model resolution is on a 2.5° x 1.9° horizontal grid with 56 vertical levels.
184 The model was run for eight years using anthropogenic emissions from the year 2000, and years
185 2006-2011 are used for analysis. Radiative feedbacks were active and allowed to feed back onto
186 climate but not meteorology. Dust entrainment processes are identical as described above for
187 CAM4. The particle size distribution differs from the bulk aerosol method with lognormal functions
188 describing the distribution via a modal aerosol model (MAM)(Liu et al., 2012). Mass mixing and
189 number mixing ratios within a given mode are predicted, with fixed geometric standard deviation
190 of each mode. Aerosol species including aerosol water are internally mixed within a mode and
191 externally mixed between modes. Dust is carried in an accumulation mode (Mode 1) and a coarse
192 mode (Mode 3) with diameter bounds at 0.1–1.0µm and 1.0-10.0µm, respectively. The particle size
193 distribution for dust entrainment was modified (default mass percents are 3.2 and 96.8% for
194 modes 1 and 3, respectively) following brittle fragmentation theory for vertical dust flux (Kok,
195 2011) with prescribed emission mass percents of 1.1 and 98.9% for modes 1 and 3. Advection and
196 deposition processes are described in Liu et al. (2012), where aerosols are represented as both
197 interstitial particles suspended in the atmosphere and as cloud-borne particles.

198 Source maps of minerals follow the mean mineralogical table (MMT) from (Claquin et al.,
199 1999), with two modifications. From the MMT, soil types whose mineral components are found not
200 to add up to 100% were gypsic xerosols and yermosols, gleyic and orthic solontchaks and salt flats
201 (Table 1). In addition to renormalizing the soil types, hematite was added to the clay fraction (0-
202 2µm) with the same proportion as prescribed in the silt fraction (2-50µm) by subtracting the
203 required fraction from illite (Balkanski et al., 2007).

ras486 11/17/14 3:13 PM

Deleted: ;Hurrell et al., in press))

Mineralogy was mapped on FAO/UNESCO WGB84 at 5' x 5' arc minutes with soil legend from FAO/UNESCO Soil Map of the World (1976; File Identifier: f7ccd330-bdce-11db-a0f6-000d939bc5d8) (Batjes, 1997). The corresponding mineral maps were regridded to model resolution (2.5° x 1.9°) (Figure 1). A nearest neighbor algorithm was applied to estimate mineralogy of land mass not specified by the soils in Claquin's MMT to allow non-zero dust emissions in these regions. As described in more detail in the following section, the clay-sized soils (0-2µm) and silt-sized soils (2-50µm) are distributed in the four CAM4 bins and two CAM5 modes following brittle fragmentation theory (Kok, 2011) (Table 2).

2.2 Conversion of soil mineralogy to aerosol mineralogy:

We model the conversion of soil mineralogy to dust aerosol mineralogy for a given transport particle size bin by following the brittle fragmentation theory of dust emission (Kok, 2011). This theory predicts that the production of dust aerosols with size D_d is proportional to the volume fraction of soil particles with size $D_s \leq D_d$ according to Equation 2,

$$\frac{dV}{dD_d} \propto \int_0^{D_d} P_s(D_s) dD_s \quad (2)$$

where V is the normalized volume of dust aerosols with size D_d and $P_s(D_s)$ is the particle size distribution of fully disaggregated soil particles. For a mineralogy data set with clay (0-2 µm diameter) and silt (2-50 µm diameter) soil fractions, we use Equation 2 to convert from soil mineralogy to dust aerosol mineralogy. More specifically, for a given aerosol with size D_d the mass fraction originating from the soil clay and silt particle fractions are given by Equation 3a and 3b respectively,

$$f_{clay}(D_d) = \int_0^{D_{clay}} P_s(D_s) dD_s / \int_0^{D_d} P_s(D_s) dD_s, \quad (3a)$$

$$f_{silt}(D_d) = \int_{D_{clay}}^{D_d} P_s(D_s) dD_s / \int_0^{D_d} P_s(D_s) dD_s \quad (3b)$$

where $D_{clay} = 2 \mu m$, $f_{clay} + f_{silt} = 1$, and $D_d > D_{clay}$. When $D_d < D_{clay}$, $f_{clay} = 1$ and $f_{silt} = 0$. The integrals in (Equation 3a,3b) are evaluated by assuming that the size distribution of fully-disaggregated soil particles follows a log-normal distribution (Kolmogorov, 1941) according to Equation 4,

$$P_s(D_s) = \frac{1}{D_s \sqrt{2\pi} \ln(\sigma_s)} \exp \left\{ -\frac{\ln^2(D_s/\bar{D}_s)}{2 \ln^2(\sigma_s)} \right\} \quad (4)$$

where \bar{D}_s is the median diameter by volume and σ_s is the geometric standard deviation. Measurements of the particle size distribution of arid soil indicate that $\bar{D}_s \approx 3.4 \mu m$ and $\sigma_s \approx 3.0$ for fully-disaggregated soil particles with diameters smaller than $20 \mu m$ (Kok, 2011). Combining Equations 3 and 4 yields,

$$f_{clay}(D_d) = \frac{1 + \operatorname{erf} \left[\frac{\ln(D_{clay}/\bar{D}_s)}{\sqrt{2} \ln(\sigma_s)} \right]}{1 + \operatorname{erf} \left[\frac{\ln(D_d/\bar{D}_s)}{\sqrt{2} \ln(\sigma_s)} \right]}, \quad (5a)$$

$$f_{silt}(D_d) = \frac{\operatorname{erf} \left[\frac{\ln(D_d/\bar{D}_s)}{\sqrt{2} \ln(\sigma_s)} \right] - \operatorname{erf} \left[\frac{\ln(D_{clay}/\bar{D}_s)}{\sqrt{2} \ln(\sigma_s)} \right]}{1 + \operatorname{erf} \left[\frac{\ln(D_d/\bar{D}_s)}{\sqrt{2} \ln(\sigma_s)} \right]} \quad (5b)$$

To obtain the fraction of dust aerosol mass originating from the soil's clay and silt fractions for a given particle size bin, Equations 5a and 5b are integrated over the bin's size boundaries and weighted by the sub-bin distribution following,

$$f_{clay,bin} = \int_{D_-}^{D_+} f_{clay}(D_d) \frac{dV}{dD_d} dD_d / \int_{D_-}^{D_+} \frac{dV}{dD_d} dD_d \quad (6a)$$

$$f_{silt,bin} = \int_{D_-}^{D_+} f_{silt}(D_d) \frac{dV}{dD_d} dD_d / \int_{D_-}^{D_+} \frac{dV}{dD_d} dD_d \quad (6b)$$

where D_- and D_+ are the lower and upper bin size limits and dV/dD_d is the sub-bin dust size distribution by volume. As previously stated, the sub-bin size distribution in CAM follows a log-

normal distribution with mass median diameter of 3.5 μm and geometric standard deviation of 2.0 (Zender et al., 2003; Reid et al., 2003). We use equations (4)—(6) to calculate the contribution of the silt and clay soil fractions to each of the 4 dust aerosol size bins used by CAM4 (Table 2a) and each of the 2 modes used by CAM5 (Table 2b).

243

244 2.3 Modeling of radiation:

Radiation in CAM4 is parameterized using the delta-eddington approximation (Joseph et al., 1976; Coakley Jr et al., 1983) to determine the reflectivity and transmissivity for each of 19 shortwave spectral intervals at each vertical layer in the atmosphere. The vertical layers at a given spectral interval are combined to account for scattering between layers, allowing for the computation of upward and downward fluxes between each layer once per model hour. The optical properties for each aerosol species including extinction and single scattering albedo in solar short wavelengths (SW) are calculated offline from species refractive indices with a Mie solver (Wiscombe, 1980) by integrating the extinction and scattering efficiencies over the size distribution of aerosol surface area. The mineral species whose SW optical properties have been derived from their respective refractive indices are illite, kaolinite, montmorillonite and hematite (Table 3) with the remaining mineral species, quartz, gypsum, feldspar and calcite being represented by a “rest of dust” blend with optics calculated with Maxwell-Garnett (Niklasson et al., 1981) mixing of 48% quartz, 25% illite, 25% montmorillonite and 2% calcite by volume (Zender, C., personal communication, 2013). The wavelength dependent complex refractive indices for all eight minerals along with the “rest of dust” blend (“Zender,” Table 3) with (Mahowald et al., 2006) and without hematite (this study) are provided in the supplementary material (S2). The density of each mineral is explicitly included ($\rho_{\text{illite}} = 2750 \text{ kg/m}^3$, $\rho_{\text{kaolinite}} = 2600 \text{ kg/m}^3$, $\rho_{\text{montmorillonite}} = 2350 \text{ kg/m}^3$, $\rho_{\text{quartz}} = 2660 \text{ kg/m}^3$, $\rho_{\text{calcite}} = 2710 \text{ kg/m}^3$, $\rho_{\text{hematite}} = 5260 \text{ kg/m}^3$, $\rho_{\text{feldspar}} = 2560 \text{ kg/m}^3$, $\rho_{\text{gypsum}} = 2300 \text{ kg/m}^3$), while the density of the “rest of dust” blend is 2500 kgm^{-3} . Hygroscopicity for all minerals as well as the dust blend is prescribed at 0.068. While different mineral species have unique water uptake abilities and thus different hygroscopicities, we assume the effect on the optical properties

ras486 11/18/14 11:10 AM

Deleted: ((Maxwell-Garnett, 1904)

ras486 11/18/14 11:10 AM

Deleted: , 2013).).

ras486 11/18/14 11:09 AM

Formatted: Font:+Theme Body, Bold, Font color: Red

268 is small compared to other factors influencing our estimate of radiative forcing, and examining the
 269 CCN/IN capabilities of minerals was beyond the scope of this study. Not all the mineral species
 270 were modeled optically because the number of mineral species included in CAM5 differs from
 271 CAM4. Thus we only include the optical properties for minerals common to both atmosphere
 272 models. A method for calculating optical properties at infrared wavelengths (LW) was not available
 273 at the time of the simulations. In CAM4, the LW aerosol effects are ignored in the release version,
 274 and are generally very difficult to calculate accurately, which is one of the many advantages of the
 275 new radiation scheme inside CAM5. We do not have a method to calculate the LW optics in CAM4 so
 276 we have to use the LW optics from CAM3 (Mahowald et al., 2006). In place of LW optical properties
 277 for the minerals, CAM3 optics were derived from refractive indices of a dust blend provided by
 278 Zender, C. S., assuming Maxwell-Garnett mixing of 47.6% quartz, 25% illite, 25% montmorillonite,
 279 2% calcite and 0.4% hematite by volume, with density = 2500 kgm⁻³ and hygroscopicity prescribed
 280 at 0.14. The error associated with this assumption is difficult to assess but may be quite large since
 281 the different minerals have very different optical properties in the longwave.

282 Radiation in CAM5.1 is parameterized with Rapid Radiative Transfer Model for GCM
 283 (RRTMG) (Liu et al., 2012; Iacono et al., 2008) with 14 and 16 spectral bands in SW and LW
 284 respectively. Mineral optical properties are parameterized by wet refractive index and wet surface
 285 mode radius, with the wet refractive index estimated using the volume mixing rule for all
 286 components including water, and the wet radius estimated from the dry radius, relative humidity,
 287 and volume mean hygroscopicity using Kohler theory (Ghan and Zaveri, 2007). Since this
 288 parameterization only utilizes refractive indices, the LW absorption parameters were generated.
 289 Flux calculations are done once per model hour for shortwave and longwave flux during model day
 290 ($\cos(\theta_0) > 0$).

291 The direct radiative forcing from dust for all simulations is determined by calculating the
 292 radiative forcing twice at each time step, one time through with all aerosol species and an
 293 additional time through with everything but dust or minerals, recalculating the wet size and volume
 294 mean refractive index without mineral dust. Both atmosphere models neglect scattering at infrared

ras486 11/17/14 3:13 PM

Deleted: place of

ras486 11/17/14 3:13 PM

Deleted: optical properties for the minerals, CAM3

ras486 11/17/14 3:13 PM

Deleted: were used (Mahowald et al., 2006), which were computed

ras486 11/17/14 3:13 PM

Deleted: ,

ras486 11/17/14 3:13 PM

Deleted:

ras486 11/17/14 3:13 PM

Deleted: kg/m³

ras486 11/17/14 3:13 PM

Deleted:

ras486 11/17/14 3:13 PM

Deleted: .

ras486 11/18/14 11:10 AM

Formatted: Indent: First line: 0.5"

ras486 11/17/14 3:13 PM

Deleted: .

306 wavelengths (LW) and only account for absorption in LW for mineral aerosols, which may
307 underestimate radiative forcing at the top of the atmosphere and surface by up to 50% and 15%,
308 respectively (Dufresne et al., 2002).

309 CAM5 was modified to include five mineral tracers for each of the two modes, four minerals
310 and an additional tracer to carry the rest of dust. As previously mentioned, neglecting the radiative
311 properties of the additional minerals in CAM4 facilitated a comparison between CAM4 and CAM5.

312 ~~In effect, we have a few extra diagnostic traces in our CAM4 simulation with mineralogy, which do~~
313 ~~not impact the simulation, and can use these in the mineralogical comparisons. However, their~~
314 ~~optical properties are identical to the “rest of dust” tracer in CAM5 and do not impact the radiative~~
315 ~~forcing differently.~~

316

317 2.4 Description of Simulations

318 The cases simulated for both CAM4 and CAM5 are listed in Table 4. CAM4-d and CAM5-d
319 simulations use dust from release versions of CAM4 and CAM5 in the CESM. CAM4-t and CAM5-t
320 simulations consist of a variety of optimizations from the default versions to better simulate
321 observed dust emission, transport, depositional fluxes and optical properties. The tuning consists
322 of optimized soil erodibility maps for each model (Mahowald et al., 2006; Albani et al., 2014),
323 emission particle size distribution following brittle fragmentation theory (Kok, 2011), increased
324 solubility for dust, increased cloud scavenging coefficients (Albani et al., 2014) and improved
325 optical properties. The improved optical properties in CAM4 include SW extinction and scattering
326 coefficients derived from the refractive indices from Maxwell-Garnett mixing of 47.6% quartz, 0.4%
327 hematite, 25% illite, 25% montmorillonite and 2% calcite by volume, with density = 2500 kgm⁻³ and
328 hygroscopicity = 0.068, and CAM3 LW absorption coefficients (Mahowald et al., 2006) computed
329 from refractive indices with Maxwell-Garnett mixing of 47.6% quartz, 25% illite, 25%
330 montmorillonite, 2% calcite and 0.4% hematite by volume, with density = 2500 kg/m³ and
331 hygroscopicity prescribed at 0.14. The inclusion of the CAM3 LW absorption coefficients is a
332 marked improvement in physical processes from release dust (CAM4-d), which has zero LW optics

ras486 11/17/14 3:13 PM

Deleted: The fewer tracers in CAM5 were simply for computational efficiency;

ras486 11/17/14 3:13 PM

Deleted: capability to add the additional minerals included in CAM4 is feasible

ras486 11/17/14 3:13 PM

Deleted: future simulations may involve including

ras486 11/17/14 3:13 PM

Deleted: ;Albani et al., submitted))

(Yoshioka et al., 2007). The optimized optical properties in CAM5 include extinction, scattering and absorption parameterizations derived from the wet particle mode radius and refractive indices from Maxwell-Garnett mixing of 47.6% quartz, 0.4% hematite, 25% illite, 25% montmorillonite and 2% calcite by volume, with density = 2500 kgm⁻³ and hygroscopicity = 0.068. The tuning parameterizations are described in detail in Albani et al., 2014, and were used for both tuned and mineralogy runs in CAM4 and CAM5. The only change from the default release for CAM we tested explicitly was the particle size distribution at emission (Kok, 2011). CAM4-m and CAM5-m simulations employ the same tuning parameterizations as the tuned cases except the optical properties (extinction and scattering for CAM4, extinction, scattering and absorption for CAM5) are derived from the mineral refractive indices (Table 3), and the emissions are scaled by the mineral maps described in sections 2.1 and 2.2 (Figure 1). Two sensitivity studies are also undertaken in order to quantify the importance of including mineralogy in place of dust in a global model for RF calculations. The studies involve characterizing the sensitivity of dust RF to the size distribution at emission (CAM4-trs, CAM5-trs) and to the soil size distribution of hematite (CAM4-mH, CAM5-mH). For the first sensitivity study, the tuning parameterizations for dust in both CAM4 and CAM5 are kept constant except the new size distribution was replaced with the size distribution in the release version of the model with mass fractions of 3.8, 11.1, 17.2 and 67.8% for bins 1-4 (CAM4-trs) and mass fraction of 3.2 and 96.8% for modes 1 and 3 (CAM5-trs). Note that hematite in the models is treated in both fine and coarse modes as the particle size distribution of hematite may differ from the (Claquin et al., 1999) MMT case where hematite was prescribed solely in the coarse mode (CAM4-m, CAM5-m). While it was acknowledged that the available data on hematite was very limited, recent observations suggest that hematite is predominantly in the smaller, clay-sized range. Cwiertney et al., (2008) finds much higher relative iron concentrations in particles < 0.75µm diameter. Higher iron concentrations indicate iron rich oxides/hydroxides as opposed to iron substitutions in silicate clay lattices, which are typically quite small (Journet et al., 2008). The second study is designed to test the sensitivity of the soil size distribution of hematite and retains all parameterizations for the mineralogy runs with the exception of removing hematite from the silt

ras486 11/17/14 3:13 PM

Deleted:

ras486 11/17/14 3:13 PM

Deleted: 0.0385, 0.111, 0.172

ras486 11/17/14 3:13 PM

Deleted: 0.678

ras486 11/17/14 3:13 PM

Deleted: fractions 0.032

ras486 11/17/14 3:13 PM

Deleted: 0.968

ras486 11/17/14 3:13 PM

Deleted:

ras486 11/17/14 3:13 PM

Deleted: (Cwiertny et al., 2008) finds much higher relative iron concentrations in particles < 0.75µm diameter.

sized soil maps and scaling up the remaining silt sized minerals (CAM4-mH and CAM5-mH). All the simulations use GEOS-5 reanalysis meteorology and were run from 2004-2011 with the last six years (2006-2011) used for analysis.

2.5 Comparison to observations

The following sections describe the comparison of mineralogy to in situ field measurements as well as ocean core sediment data (Table 5). Distinguishing natural mineral aerosol is complicated by atmospheric mixing with anthropogenic aerosols and other natural aerosols, as well as the distance between the dust source and the location of the observations (Claquin et al., 1999; Kalashnikova and Kahn, 2008). Additionally, ocean sediment measurements are complicated by complex ocean circulation patterns (Han et al., 2008; Siegel and Deuser, 1997). A wide variety of methods are used for dust sample collection; this can impact measuring concentrations of smaller or highly aspherical particles (Reid et al., 2003), the non-uniformity of which further complicates the model verification process. As a way to compare observed mineralogy where particle size distribution is not explicitly reported, the mass ratio of minerals with similar diameters are compared to the mass ratios of observed mineralogy (Claquin et al., 1999).

The mixing ratio of minerals near the surface in CAM4 and CAM5 is compared to the only available observation (Kandler et al., 2009) of relative mineral volume abundance as a function of mean particle diameter (Figure 4). Kandler et al. (2009) reports mineral fractions with particle diameters that do not match the modeled particle diameter for Bin 1 in CAM4 and Modes 1 and 3 in CAM5. To compare the observed mineral fractions to the model, after converting observed volume fractions to mass fractions, the average mass abundance for CAM4 bin1 was related to particle diameters 0.16, 0.35 and 0.71 μm (Equations 7 and 8).

$$\bar{\gamma}\rho = \frac{\int_{0.1}^{D_{1,+}} \frac{dV}{dD_d} \gamma_1 dD_d + \int_{D_{2,-}}^{D_{2,+}} \frac{dV}{dD_d} \gamma_2 dD_d + \int_{D_{3,-}}^1 \frac{dV}{dD_d} \gamma_3 dD_d}{\int_{0.1}^1 \frac{dV}{dD_d} dD_d} \quad (7)$$

400 Where

$$\frac{dV}{dD_d} = \frac{1}{c_v} \left[1 + \operatorname{erf} \left(\frac{\ln(D_d/\bar{D}_s)}{\sqrt{2} \ln(\sigma_s)} \right) \right] \exp \left[- \left(\frac{D_d}{\lambda} \right)^3 \right] \quad (8)$$

401 The upper and lower diameters are the middle of the particle diameters reported in Kandler et al.
 402 (2009); $D_{1,+} = D_{2,-} = (D_1 * D_2)^{0.5} = 0.24 \mu\text{m}$, $D_{2,+} = D_{3,-} = (D_2 * D_3)^{0.5} = 0.5 \mu\text{m}$. V is the normalized volume
 403 of dust aerosols with size D_d , $c_v = 12.62 \mu\text{m}$ is a normalization constant, ρ is the density of a given
 404 mineral, and γ_{1-3} are the observed volume fractions at 0.16, 0.35 and $0.71 \mu\text{m}$ respectively.
 405 Equation 8 is the predicted size distribution at emission following brittle fragmentation theory
 406 (Kok, 2011). The size distribution at emission and the distribution observed for particles of
 407 diameters $< 1.0 \mu\text{m}$ are expected to be similar given the proximity of the measurements to the
 408 emission source as well as the negligible impact of gravitational settling. Particle diameters 1.6, 3.5
 409 and $7.1 \mu\text{m}$ correspond well with bins 2-4, respectively. For CAM5, the accumulation mode was
 410 matched with the correlation for bin 1 and the coarse mode average mass fraction of mineral
 411 species was estimated from Equations 9 and 10.

412

$$\bar{\gamma}\rho = \frac{\int_1^{D_{1,+}} \frac{dV}{dD_d} \gamma_1 dD_d + \int_{D_{2,-}}^{D_{2,+}} \frac{dV}{dD_d} \gamma_2 dD_d + \int_{D_{3,-}}^{10} \frac{dV}{dD_d} \gamma_3 dD_d}{\int_1^{10} \frac{dV}{dD_d} dD_d} \quad (9)$$

413 where

$$\frac{dV}{dD_d} = \left[0.5 + 0.5 \operatorname{erf} \left(\frac{\ln(D_d/\bar{D}_{pg})}{\sqrt{2} \ln(\sigma_g)} \right) \right], \quad (10)$$

414 is the size distribution at emission. The upper and lower diameters are the middle of the particle
 415 diameters reported in Kandler et al. (2009); $D_{1,+} = D_{2,-} = (D_1 * D_2)^{0.5} = (1.6 * 3.5)^{0.5} = 2.4 \mu\text{m}$, $D_{2,+} = D_{3,-}$
 416 $= (D_2 * D_3)^{0.5} = (3.5 * 7.1)^{0.5} = 5.0 \mu\text{m}$.

417 Comparing the modeled distribution of minerals with observations that do not specify the
 418 particle size distribution is not very effective since there is a correlation between mineralogy for a
 419 given particle size distribution (Claquin et al., 1999). For this reason, the ratio of similarly-sized
 420 minerals is compared. The following mineral ratios were chosen because they matched the similar

size criterion and had at least five locations of observation. In the clay-size range, kaolinite to illite (K/I) is chosen because this comparison was possible for both CAM4 and CAM5. In the silt-size range, the following comparisons were made: calcite to quartz (C/Q) and feldspar to quartz (F/Q).

3.0 Results:

3.1 Desert dust mineralogical distribution

The spatial distribution of minerals in [aerosols in](#) CAM4 and CAM5 are different (Figure 2 and 3) and while the distributions of minerals in soils are identical for both models (Figure 1), there are different physical parameterizations for aerosol advection and deposition between CAM4 and CAM5. In order to discuss the significance of the spatial distribution of mineralogy and to give credibility to the simulations, the modeled distributions are evaluated with available observational data (Table 5).

Because of the size segregation of minerals in the soil materials (Claquin et al., 1999), it is ideal to compare the modeled mineralogy by size distribution. However, there is limited size segregated data (Table 5; Figure 4). For four of the seven minerals considered from Kandler et al., 2009—illite (Figure 4a), kaolinite (Figure 4b), quartz (Figure 4c) and feldspar (Figure 4f)—the simulations for both CAM4 and CAM5 simulate dynamic range in mineral mass fraction with particle size, while the mass fractions observed are relatively constant with size. This is because in the simulations we assumed that the clay-sized minerals dominate the smaller size bins while the silt-sized minerals dominate the larger size bins. While the magnitude of gravitational settling for any given mineral is larger in the coarser bins, the relative mass for finer bins (1 and 2) is dominated by clay minerals and the relative mass for coarser bins (3 and 4) is dominated by silt-sized minerals. The proximity of the observation to the source of emission is another possible explanation for why the relative fractions sampled are constant with size, since transport and deposition haven't significantly altered the mineral distributions at emission.

There is one instance of the [range of](#) variability of mass with size where the CAM4 simulation did not predict this variability for gypsum (Figure 4g). In general, gypsum

449 concentrations predicted from Claquin's MMT were very small (Figure 1h, Figure 2h) and this may
450 cause a low bias in the model. However, Glaccum and Prospero (1980) reported gypsum
451 crystallizing on collection plates and was hence not considered to have been part of the transported
452 minerals observed during their field study. Given the discrepancies on how to measure gypsum
453 concentrations along with atmospheric processing of gypsum (Glaccum and Prospero, 1980) that
454 was not simulated in this study, the attempt to correlate gypsum observations with simulated
455 gypsum concentrations is likely not very meaningful. Calcite (Figure 4d) and hematite (Figure 4e)
456 are correlated with observations at this location, with hematite being most important for
457 simulating the DRF in the shortwave, which is one of the primary goals of this study.

458 Next we compare the ratio of minerals available in the observations (Table 5). When
459 comparing means between models and observations, we see a low bias in both models however
460 CAM5 more closely matches the mean of observations. In general, both CAM4 and CAM5 do not
461 capture the dynamic range seen in the observations (Figures 5-8) when comparing monthly mean
462 model output to the month the observations were made. For the comparison of kaolinite to illite,
463 the mean observational ratio is 0.72 ± 0.91 compared to the mean ratios for CAM4 and CAM5 of
464 0.55 ± 0.18 and 0.63 ± 0.28 respectively. K/I in CAM5 indicates some structure and range in
465 possible values; however the sites of observation are all in the N. Hemisphere, except for one site in
466 Australia, limiting comparisons where CAM5 predicts greater range (Figure 5). The daily averaged
467 mineral ratios for all days simulated indicates temporal variability on the same order of magnitude
468 as the variability in the observations, suggesting that temporal variability can be playing a
469 significant role in the observed ratios. The silt-size mineral ratios are only compared for CAM4
470 since quartz is not explicitly modeled in CAM5 (Figure 6). The mean in the observations for the
471 ratios calcite to quartz and feldspar to quartz are 0.56 ± 0.26 and 0.42 ± 0.22 respectively and the
472 means for CAM4 C/Q and F/Q are 0.32 ± 0.08 and 0.32 ± 0.09 respectively. Similarly to K/I, figures
473 7 and 8 indicate the inability of the model to capture the range of variability of observed ratios
474 when comparing monthly means and some improvement when looking at daily averages.

476 Typically, dust samples from field studies are collected during a dust event over a period of
477 1-3 days. Since the observations were made at various time periods in the past, we have not
478 simulated the exact days the observations occurred. Instead, we compare the model simulations
479 monthly means to the month the observations were made. Therefore, while the simulated monthly
480 mineral ratios do not appear to have the range of variability from observations, this is likely at least
481 partially an artifact of the smoothing effect from monthly averages. We see an increase in
482 variability, particularly for CAM5 when examining the daily averaged mineral ratios for each day
483 from 2006-2011 (Figure 5).

484 Modeled mineral ratio K/I is compared to ocean core sediment mineralogy for CAM4
485 (Figure 7) and CAM5 (Figure 8) (Biscaye, 1965). The mean ratio in the data is 1.14 ± 3.7 and the
486 mean ratio at the observation coordinates is the same for both CAM4 (0.62 ± 0.17) and CAM5 (0.62
487 ± 0.19) indicating an underestimate of mean and variability of this ratio in both models. The
488 correlations for both models are quite poor overall, and the range in values for CAM5 is similar to
489 CAM4, with 95% of data points falling between 0.4 and 1, compared to CAM4 with a range of 0.4 to
490 0.95. Note some resemblance of the spatial pattern of Biscaye's data (Figure 7b,8b) with CAM5
491 (Figure 8a) around N. Africa and eastern S. America. The latitude band correlations for CAM4 and
492 CAM5 are poor although CAM5 appears to have more variability along the equator. While these
493 figures do not capture the range in the data, the comparison is inherently difficult given ocean
494 circulation of dust from deposition on the surface to sedimentation on the ocean floor that the
495 simulated deposition distributions cannot be expected to capture (Han et al., 2008; Siegel and
496 Deuser, 1997). This along with physical and chemical processing during atmospheric transport and
497 sedimentation further hinder the comparison.

498 Summarizing the above comparisons, the mineralogical distributions simulated by the
499 model do not have the dynamic range that the few available observations indicate. However,
500 multiple factors are responsible, from differing time scales of observations to the atmospheric
501 processing of dust that is not yet included in these models. When looking at daily averaged mineral
502 ratios (Figure 5-6), the temporal variability in the simulations indicates greater range than monthly

ras486 11/17/14 3:13 PM

Deleted: dynamic

means. In addition, there is likely to be sub-grid variability in the spatial distribution of mineralogy, which is not at all captured by the model. We also assume one mean mineralogical relationship to every soil type, which is an oversimplification. Interestingly, mineral ratios in most of the main desert soils exhibit range of variability within the range of the observations of variability in mineral concentrations. This suggests that in theory, the soil maps we are using could capture the observed ranges in mineral ratios. For example, the variability of the mineral ratio K/I in N. Africa is between about 0.2 to 5. Since there were more observations in this region accounted for in the mineral maps from Claquin et al., 1999, along with N. Africa accounting for up to 80% of global dust emission, this heterogeneity is promising. However, due to the coarse resolution of the model, the mineral ratios in the simulations do not capture observations of mineral ratios in dust deposition or concentrations near the surface. In addition, the variability over desert regions in Australia is low (between 1 and 2), while in China, nearly all grid boxes of soil mineralogy K/I are around 0.5 which suggests that the assumed soil mineral variabilities are not adequate in these regions. While in the model we include kaolinite and illite with the same assumed size distribution, in reality, kaolinite tends to be in a slightly larger size fraction than illite (0.5-4 μ m and 0.1-1 μ m, respectively) (Glaccum and Prospero, 1980). So in the model these values will tend to stay constant as the model advects them downwind, while in reality these should be more fractionation occurring with transport. It is unclear how more resolution of the size fractions of the minerals in the soils would improve our simulations. As this study was a first attempt at modeling global mineralogy and was primarily dedicated to building the framework required to carry multiple mineral tracers as well as synching them with the radiation codes, a module to simulate physical and chemical fractionation and processing of minerals during emission and transport was not available for this study. Therefore, these simulations cannot be expected to capture all the observed mineral characteristics of dust deposited away from the source. For example, observations suggest that calcite concentrations in airborne dust are a function of the wind velocity that occurred during saltation, with the relative amount decreasing with increasing velocity (Caquineau et al., 1998;Gomes et al., 1990;Sabre et al., 1997), a process that is not included here. In addition, acidic processing of calcite to gypsum would

531 also result in less calcite abundance in collected dust and an overall increase in the abundance of
532 clay. In the future, improvements to the simulation of the distribution of mineralogy, especially to
533 better capture the range of variability, are necessary.

ras486 11/17/14 3:13 PM

Deleted: dynamic

534 3.2 Aerosol optical depth and single scattering albedo

536 Annually averaged aerosol optical depth (AOD), absorbing aerosol optical depth (AAOD)
537 and single scattering albedo (SSA) (Holben et al., 1998; Holben et al., 2001; Dubovik and King,
538 2000; Dubovik et al., 2000) are simulated for each model at 533 nm and compared to annually
539 averaged AERONET retrievals. AERONET sites were chosen in regions where the modeled AOD_{dust}
540 $> AOD_{total} \times 0.5$ (at 533 nm) to restrict the comparison to dust. The total AOD depends on the
541 concentration of suspended aerosols and the degree to which they attenuate radiation. For both
542 CAM4 and CAM5, the simulations with mineralogy have smaller values compared to the simulations
543 with tuned dust at nearly every point (Figure 9a,b); however both tuned and speciated cases agree
544 with measurements of AOD much better than AAOD. This is due to the shortwave extinction
545 coefficients for tuned dust having higher values than the extinction coefficients for each of the
546 minerals. Both the simulations with tuned dust and with mineralogy are biased low and their range
547 is about half that observed (Figure 9a,b). The simulations with mineralogy perform worse than
548 those with tuned dust (Table 6) when comparing mean and range for AOD. The comparison for
549 AAOD is poor for the tuned and mineralogy simulations with CAM4 however CAM5-m matches
550 observations reasonably well with a predicted range larger than observed (Table 6b). CAM4-t and
551 CAM5-t are more accurate at capturing the mean observed SSA across many sites while CAM4-m
552 performs worse than CAM5-m (Figure 9e,f). CAM4-m SSA is biased high and has decreased range of
553 variability and less correlation than CAM4-t (Table 6). CAM5 overall is dustier with 8.2% of
554 gridcells meeting $AOD_{dust} > 0.5 \times AOD_{total}$, and 27.5% of these have column hematite percents greater
555 than 1.5%. In contrast, CAM4-m has 56% fewer “dusty” gridcells with only 17.6% of these
556 containing total column hematite percents above 1.5%. While CAM5-t does well in matching
557 AERONET SSA. CAM5-m predicts lower SSA and a greater range than observed (Figure 9f).

ras486 11/17/14 3:13 PM

Deleted: 533nm

ras486 11/17/14 3:13 PM

Deleted: 533nm

561 Adding mineralogy to CAM4 does not seem to improve the simulation of AERONET AOD,
 562 AAOD, and SSA, whereas it does marginally in CAM5. Adding mineralogy to CAM5 adds to the
 563 quality of the simulation at the AERONET sites because of the higher amounts of dust, as well as
 564 more hematite (Figure 10 and 11). Black carbon is a more efficient absorber than hematite (SSA =
 565 0.17 vs. 0.6, for black carbon and hematite, respectively). Black carbon is twice as abundant in
 566 CAM4-m as in CAM5-m in dust-dominated regions and it dominates the SSA signal (Figure 10 and
 567 11). The lower black carbon concentrations may be due to the internal mixture assumption for BC
 568 in CAM5 (Wang et al., 2013). Recognize that while the aerosol forcing datasets and meteorology
 569 were the same for both simulations, the simulations of CAM4 and CAM5 have many differences,
 570 including physical parameterizations for aerosol transport and deposition along with different
 571 radiation schemes. Overall, inclusion of mineralogy did not improve comparisons at AERONET
 572 stations for AOD, AAOD and SSA.

573

574 3.3 Radiative Forcing

575 3.3.1 Clear-sky radiative forcing

576 The TOA radiative forcing efficiency ($\text{Wm}^{-2}\tau^{-1}$) of dust is compared to clear-sky satellite
 577 based observations over N. Atlantic (Li et al., 2004) and the Sahara (Zhang and Christopher,
 578 2003; Patadia et al., 2009) for both simulations with tuned dust and mineralogy in CAM4 and CAM5
 579 (Table 7). Out of the three shortwave observations considered, CAM4-t matches two of the
 580 observations better than CAM4-m. The clear-sky forcing efficiency observed by Li et al. 2004
 581 during June, July and August (JJA) over the N. Atlantic is captured by CAM4-t, while CAM4-m
 582 simulated a smaller forcing. The extinction coefficient of tuned dust is larger than that of individual
 583 minerals; the refractive indices of tuned dust were calculated based on Maxwell-Garnet internal
 584 mixture of non-absorbing clays and quartz and absorbing hematite. The real part (scattering) and
 585 the imaginary part (absorbing) of the refractive index at 533 nm is larger for tuned dust than for
 586 each of the minerals except for the real part in montmorillonite and for hematite, (dust($\lambda=533$ nm):
 587 1.515 - i0.00236, illite($\lambda=533$ nm): 1.415 - i0.00103, kaolinite($\lambda=533$ nm): 1.493 - i9.954e-5,

ras486 11/17/14 3:13 PM

Deleted: portion

ras486 11/17/14 3:13 PM

Deleted: portion

ras486 11/17/14 3:13 PM

Deleted: 533nm are

ras486 11/17/14 3:13 PM

Deleted: .

592 montmorillonite($\lambda=533$ nm): 1.529 – $i0.00185$, hematite($\lambda=533$ nm): 2.967 – $i0.7997$, rest of dust
 593 blend($\lambda=533$ nm): 1.51 – $i0.00105$). Hematite has much larger imaginary and real parts however
 594 the density of hematite is twice as large as the densities for tuned dust and for each of the minerals.
 595 Since the mass extinction efficiency is a factor of 1/density, hematite has a smaller mass extinction
 596 efficiency than all other minerals. The reason that CAM4-m has a smaller forcing efficiency is that
 597 for similar dust and mineral loads, the amount of radiation scattered back to space is dominated by
 598 the greater extinction efficiency of tuned dust, e.g. tuned dust results in 13% more extinction per
 599 unit mass than mineralogy. For the “low” dust season, November, December and January (NDJ), the
 600 same phenomena is found: with similar dust and mineral loads, tuned dust results in a more
 601 negative forcing efficiency at TOA for the CAM4-t case. However in this case, CAM4-m more closely
 602 matches the observation; however, the significance of this is not clear as clear-sky measurements
 603 during winter may be capturing black carbon from biomass burning as well as dust (Li et al., 2004).
 604 CAM5-m underestimates the SW forcing efficiency observed by Li et al. (2004) while CAM5-
 605 t more closely matched this (Table 7). The reason for this is that mineralogy is significantly more
 606 absorbing with higher column concentration of hematite, despite similar loadings and optical
 607 depths (Figure 16). Over the same domain but for the low dust season, the mineralogy simulation
 608 more closely matches the observation, most likely from the more absorbing mineralogy compared
 609 to the tuned dust. While both mineralogy simulations (CAM4-m and CAM5-m) fall within the range
 610 of the observation for NDJ season, the dust loading differs between these, 0.38 and 0.26Tg
 611 respectively with optical depths 0.054 and 0.046. The extinction per mass is higher for CAM5-m
 612 however since CAM5-m is also more absorbing than CAM4-m, the resulting RFE’s are similar.
 613 The clear-sky forcing efficiency over North Africa is approximately 0 in the observations for
 614 a surface albedo of 0.4 during “high” dust season (JJA) (Patadia et al., 2009). Both CAM4 and CAM5
 615 simulations with tuned dust match the observations better than the simulations with mineralogy.
 616 Over N. Africa, there are competing mechanisms for the TOA forcing efficiency in both reality and
 617 modeling. Tuned dust in CAM4 is more absorbing than CAM4-m however it is also more efficient at
 618 scattering incoming SW radiation. In addition to scattering more incoming radiation (cooling at

ras486 11/17/14 3:13 PM

Deleted: portions

TOA), it will also absorb more SW radiation reflected from the surface (warming at TOA). CAM4-m is not as efficient at scattering incoming solar radiation and results in less cooling at the surface. Since TOA forcing is the sum of forcing at the surface and in the atmosphere, the smaller cooling from CAM4-m and similar atmospheric heating for both CAM4-t and CAM4-m results in an increased positive forcing at TOA for CAM4-m. In CAM5, the simulation with mineralogy has relatively high concentrations of hematite in this region (Figure 3d, Figure 11a) hence low SSA (Figure 16d), and absorbs both incoming solar radiation and reflected SW radiation; for similar loads and optical depths, CAM5-m simulates increased surface cooling and four times as much heating in the atmosphere, explaining the net positive SW forcing at TOA.

Both CAM4 and CAM5 underestimate the clear-sky LW forcing efficiency observed by Zhang and Christopher (2004) over N. Africa in September. The difference between CAM4-m and CAM4-t is not meaningful since the same LW optical properties were prescribed for both tuned dust and mineralogy. CAM5-m does worse than CAM5-t for this observation. For CAM5-m, the clay minerals and hematite were the only minerals included, and the silt-sized minerals such as quartz and calcite were not explicitly modeled. Quartz dominates absorption in the IR spectrum with additional significant contributions from both the silt-sized and clay minerals (Sokolik and Toon, 1999). CAM5-m is not capturing the quartz signal or the other silt-sized mineral signals, and thus it simulates less surface heating and a smaller LW TOA forcing. The simulations of dust and mineralogy in CAM4 and CAM5 only account for absorption in the LW and exclude scattering which has been shown to underestimate the LW forcing by up to 50% at TOA and 15% at the surface (Dufresne et al., 2002) and serves to explain why both models underestimate the observed forcing.

3.3.2 All-sky radiative forcing

All-sky radiative forcing is a delicate balance between heating and cooling of SW and LW radiation (Table 8, Figure 12-14). The difference between tuned dust and mineralogy for the all-sky TOA radiative forcing spatial distribution for CAM4 (Figure 14a,c) indicates intensified heating over desert and less cooling everywhere else. This is consistent with the more absorbing nature of tuned

ras486 11/17/14 3:13 PM

Deleted: S3

648 dust whose optical properties represent an internal mixture of minerals compared with mineralogy
 649 with combined optics of the external mixing of illite, kaolinite, montmorillonite, feldspar and
 650 hematite, along with an internal mixture of calcite, montmorillonite, quartz and illite; the result for
 651 CAM4-t being increased surface cooling with nearly identical atmospheric forcings and an overall,
 652 albeit small, net cooling compared to the small overall net warming from CAM4-m. On the other
 653 hand, the spatial pattern for CAM5-m indicates an intensification of heating over source regions,
 654 largely due to the SW atmospheric heating from hematite's absorption of both incoming and
 655 reflected SW radiation (Figure 14d, Figure 3d, Table 8b). Over bright reflective surfaces such as
 656 desert, higher column concentrations of hematite in CAM5-m absorb incoming solar radiation as
 657 well as SW radiation reflected by the high-albedo surface resulting in less solar radiation being
 658 reflected back out at TOA. While the larger absorption of incoming solar radiation of CAM5-m does
 659 not change the SW forcing at TOA, the absorption of reflected SW does affect this, and over desert, it
 660 is clear that both these processes result in a positive atmospheric forcing twice as large as the
 661 cooling at the surface (Table 8b). Net surface forcing for CAM4-t, CAM4-m and CAM5-t have similar
 662 spatial patterns as TOA forcing, however, CAM5-m indicates much greater surface cooling
 663 everywhere (Figure 12). The spatial pattern of net atmospheric forcing for CAM4-t and CAM4-m
 664 are nearly identical (Figure 13a,c), arising from the very similar SSA maps (Figure 16a,c); for CAM5-
 665 m, the atmospheric heating due to both absorption of incoming and reflected SW is clearly seen
 666 compared to CAM5-t (Figure 13b,d). In the three major regions contributing to RF from dust, N.
 667 Atlantic, N. Africa, W. Indian Ocean (Yoshioka et al., 2007), the changes between mineralogy and
 668 tuned dust are dominated by SW forcing (Table 8b).

669 To summarize, there are two different mechanisms for increased positive TOA forcing for
 670 both models with mineralogy. For CAM4, while the SSA is higher for the case with explicit
 671 mineralogy, the overall extinction efficiency is higher for tuned dust, largely due to the fact that the
 672 optical properties for tuned dust are simulated as an internal mixture of illite, kaolinite, calcite,
 673 quartz and hematite. For CAM5, both dust and mineralogy is internally mixed with other aerosol
 674 species, however the SSA for mineralogy is much lower due to the high concentrations of hematite

675 over key regions contributing to the global RF from dust. While it is not clear that mineralogy
676 improves global dust RF, and in several observations appears to do worse, all four simulations fall
677 within the range of previous RF modeling estimates (Yoshioka et al., 2007; Woodward, 2001; Miller
678 et al., 2004; Miller et al., 2006).

679 A comparison to radiative forcing efficiency from another study that included mineralogy
680 (Balkanski et al., 2007) is not straightforward since that study inferred that the ideal hematite
681 inclusion for an internal dust mixture is twice the value in this study. For both CAM4 and CAM5
682 simulations with mineralogy, the hematite content in the soil distributions is 1.4% by mass, or,
683 0.7% by volume, while the tuned dust assumes 0.8% hematite by mass, or 0.4% by volume. For the
684 case with 1.5% hematite by volume, they report TOA forcing efficiency which is too cooling
685 compared to the clear-sky RFE reported by Li et al. 2004, while the simulated surface RFE matched
686 observations. From this, the atmospheric heating efficiency was underestimated. The results for
687 clear-sky TOA forcing efficiency are less cooling in both CAM4-m and CAM5-m however the surface
688 RFE in both cases is very similar to the observed $-65 \pm 3 \text{ Wm}^{-2}\tau^{-1}$, -63 and $-64 \text{ Wm}^{-2}\tau^{-1}$ respectively.
689 Additionally, both cases with mineralogy come close to the estimated atmosphere heating efficiency
690 of $30 \pm 4 \text{ Wm}^{-2}\tau^{-1}$, with values of 38 and $41 \text{ Wm}^{-2}\tau^{-1}$ for CAM4-m and CAM5-m respectively.

691

692 3.4 Sensitivity to Size

693 Changing the assumed optical properties derived from optimized refractive indices are
694 most important in determining all-sky DRF (CAM4-t, CAM5-t), with size (CAM4-trs) and mineralogy
695 (CAM4-m) following with comparable importance in CAM4 and with mineralogy (CAM5-m) and
696 then size in CAM5 (CAM5-trs)(Table 9). Comparing to clear-sky RFE observations, the order of
697 importance is less clear for CAM4 with tuned optics, scavenging and release size distribution
698 (CAM4-trs) doing worse ($-32.0 \text{ Wm}^{-2}\tau^{-1}$) than CAM4-t ($-33.9 \text{ Wm}^{-2}\tau^{-1}$) over N. Atlantic JJA and better
699 ($-32.7 \text{ Wm}^{-2}\tau^{-1}$) during NDJ than CAM4-t ($-35.9 \text{ Wm}^{-2}\tau^{-1}$) (Table 7). Comparing to observations from
700 Patadia et al. 2009, both CAM4 and CAM5 with tuned dust plus release size-distribution (CAM4-trs
701 and CAM5-trs) overcompensates the cooling efficiency while both simulations with mineralogy

702 (CAM4-m and CAM5-m) predict heating (Table 7). In general, the higher concentrations of small
703 particles in the simulations using release sizes result in increased reflectivity and increased cooling
704 at TOA. For clear-sky observations, it appears that size is more important than mineralogy, and of
705 comparable importance to optics.

706 Comparing to AERONET retrievals, root mean square errors (RMSE) are calculated for the
707 tuned dust plus release size distribution simulations (CAM4-trs and CAM5-trs) compared to the
708 RMSE for the tuned and mineralogy cases for AOD, AAOD, and SSA. For CAM4, RMSE in AOD for the
709 tuned (CAM4-t) and mineralogy (CAM4-m) simulations are similar and higher than for the tuned
710 plus release size case (CAM4-trs) (0.197, 0.152, 0.200 for CAM4-t, CAM4-trs and CAM4-m,
711 respectively). For AAOD and SSA however, RMSE for mineralogy is the highest followed by
712 identical errors for the tuned and tuned release size simulations, and by tuned plus release size
713 then tuned for AAOD (0.032, 0.032, 0.038 for CAM4-t, CAM4-trs, and CAM4-m) and SSA (0.020,
714 0.029, 0.039 for CAM4-t, CAM4-trs, and CAM4m), respectively. This indicates that when comparing
715 to AOD for CAM4, the release particle size distribution provides the best match to observations with
716 mineralogy and tuned dust approximately equal in ability. However for AAOD and SSA, mineralogy
717 has the poorest match to observations while the tuned cases with optimized size distribution and
718 with release size distribution are either equal in ability (AAOD) or the release size distribution
719 performs worse (SSA). For CAM5, RMSE for AOD is lower for each case than CAM4. The CAM5
720 simulation with tuned dust better matches observations followed by mineralogy and then tuned
721 plus release size distribution (0.112, 0.124, 0.118 for CAM5-t, CAM5-trs and CAM5-m respectively).
722 Similarly, for AAOD, the RMSE for the CAM5 simulations are all lower than for CAM4. Again, the
723 CAM5 simulation with mineralogy best matches observations followed by tuned plus release dust
724 and then tuned (0.023, 0.022, 0.015 for CAM5-t, CAM5-trs and CAM5-m, respectively). And for
725 RMSE for SSA, the simulation with mineralogy most poorly matches observations while the
726 simulation with tuned dust best matches (0.017, 0.023, 0.036 for CAM5-t, CAM5-trs, and CAM5-m,
727 respectively). Thus CAM5 better captures the variability in AERONET than CAM4 however, the
728 simulations with tuned dust and release size distribution help the comparison for CAM4 and hinder

729 it for CAM5. With the exception of AAOD in CAM5, the tuned runs overall are most accurate with
730 mineralogy and tuned plus release size distribution following, depending on the measurement in
731 question (Figure 15). Despite this, the size distribution of dust estimated from AERONET more
732 closely matches the size distribution derived from Kok, 2011 (Albani et al., 2014). Overall,
733 including mineralogy is comparable to changes in size and optics when comparing to AERONET;
734 however, when comparing to radiative forcing, it is less clear whether including mineralogy is as
735 important as optics or size changes.

736

737 3.5 Sensitivity to soil distribution of hematite:

738 Testing whether or not including hematite only for the soil clay and not for soil silt made no
739 difference for CAM4; hematite concentrations were already low enough, particularly over dust
740 source regions (Figure 2f) where removing the hematite from the silt-sized soils didn't have an
741 impact on DRF, RFE observations or comparisons to AERONET retrievals (Table 6a,b,7,8a, Figure
742 15, S2a,c).

743 On the other hand, this sensitivity test was more interesting for CAM5. Comparing to
744 AERONET retrievals of AAOD and SSA (Table 6a,b), excluding hematite from the coarse soil fraction
745 (CAM5-mH) does better than including it (CAM5-m). While the mean AAOD for the case without
746 coarse hematite (CAM5-mH) differs more than including it (CAM5-m), the variability is closer to the
747 observed variability. And for SSA, the mean SSA for the case without coarse hematite (CAM5-mH) is
748 closer than CAM5-m to the mean in AERONET, with the variability coming even closer to the
749 observed variability. When comparing to the observations of clear-sky RFE, in all cases except for
750 the LW observation, the case without coarse hematite (CAM5-mH) does better than the case with
751 both fine and coarse hematite (CAM5-m) in matching these observations (Table 7). Finally, when
752 examining the all-sky DRF, while the surface forcings for the case with both fine and coarse
753 hematite (CAM5-m) and without coarse hematite (CAM5-mH) are very similar, the reduction of
754 atmospheric heating for CAM5-mH is tempered by the smaller overall hematite concentration,
755 particularly close to source regions where there are fewer large hematite particles able to absorb

ras486 11/17/14 3:13 PM

Deleted: et al.

ras486 11/17/14 3:13 PM

Deleted: submitted

ras486 11/17/14 3:13 PM

Deleted: S4a

759 radiation. And therefore, at TOA, the sign changes from slightly positive for CAM5-m, $+0.05 \text{ Wm}^{-2}$
760 to slightly negative for CAM5-mH, -0.04 Wm^{-2} . (Table 8a). The spatial patterns for the mineralogy
761 simulations with and without coarse hematite (CAM5-m and CAM5-mH respectively) are similar
762 and indicate an intensification of heating over source regions, largely due to the SW atmospheric
763 heating from hematite's absorption of both incoming and reflected SW radiation (Figure [S2d](#), Figure
764 [13d](#), Figure 3d, Table 8a). The positive atmospheric forcing for CAM5 with hematite in both the fine
765 and coarse modes (CAM5-m) is three times as large as for the simulation with tuned dust (CAM5-t),
766 it is a little over twice as large for the mineralogy case without coarse hematite (CAM5-mH), with
767 the balance between the lesser atmospheric forcing combined with the similar surface cooling
768 being sufficient to change the sign at TOA for CAM5-mH (Table 8a). Our results suggest that
769 excluding the coarse mode hematite is more realistic, which is similar to the methodology proposed
770 in a new mineralogy map (Journet et al., 2014).

771

772 3.6 Quantifying Uncertainty:

773 As this study is the first we are aware of to simulate the radiative forcing by modeling the
774 distribution of individual minerals in place of dust, it is not possible to compare the uncertainties in
775 our model with those from another study. In an attempt to quantify the uncertainties associated
776 with the mineralogy simulations, we identify the sources of error to estimate an upper bound
777 uncertainty. From the mineral source maps derived from Claquin et al. 1999, the standard
778 deviation in soil mineral content comprises up to 33% of the given mineral contents. Uncertainties
779 from direct radiative forcing of dust based on simulations included in the Intergovernmental Panel
780 on Climate Change (IPCC) have been previously estimated to be around 20% (Mahowald et al.,
781 2010), which results from a combination of the uncertainty associated with dust distribution and
782 the radiative forcing calculation itself. We do not have enough data to estimate the uncertainties in
783 the mineral optical properties, although it is clear that the refractive indices for a given mineral can
784 vary due to imperfections or inclusions which may reflect the geographic location of minerals. [For](#)
785 [example, chemical composition can vary between two samples collected at a single location, and](#)

ras486 11/17/14 3:13 PM

Deleted: S4,d,

ras486 11/17/14 3:13 PM

Deleted: 14d

788 | have different refractive indices (Egan and Hilgeman, 1979). Additionally, two samples of the same
789 | mineral from different geographic locations can also have different refractive indices (Egan and
790 | Hilgeman, 1979). Therefore, we are only able to make a rough estimate of the uncertainty in the
791 | direct radiative forcing from mineralogy, which could be greater than 50%. The ability to reduce
792 | the uncertainty is limited by available mineralogy maps, and having the mineralogy at every
793 | location is currently not feasible even with remote sensing. Daily averaged values for
794 | mineralogical data show large temporal variability in mineral ratios (Figures 5 and 6), but spatial
795 | variability due to sub-grid scale mineralogical heterogeneity could be as large or larger, and is not
796 | assessed here. Effectively evaluating the mineralogy temporal and spatial variability could be
797 | achieved but only with many more current observations of mineralogy, and in particular
798 | observations of mineralogy as a function of particle size distribution.

799

800 Discussion and Conclusion:

801 | For the first time, the ability to carry multiple types of minerals instead of only a bulk dust
802 | has been included in both CAM4 and CAM5, and mineralogy is coupled to radiation to simulate the
803 | impacts on radiative forcing. In general, the mineral distributions simulated in CAM4 and CAM5
804 | lack the range of variability that the few available observations indicate, although this is improved
805 | when daily averaged values are compared instead of monthly means. Myriad reasons are
806 | responsible, including the averaged mineral source maps used in the simulations, the very limited
807 | number of mineralogy observations, as well as the fact that atmospheric processing of minerals is
808 | not yet included in these models. In order to compare mineralogy collected over the course of a
809 | dust event to daily averaged model output, more current observations are needed with
810 | specification of the particle size distribution of the collected minerals. Despite the lack of
811 | observations to compare to, new mineral source maps such as from Journet et al., 2014, are needed
812 | along with chemical and physical atmospheric processing mechanisms to better compare to
813 | observations. An additional difficulty arises from soil properties and mineralogy that change on
814 | very short spatial scales in the real world, while the model assumes averages over large regions.

ras486 11/17/14 3:13 PM

Deleted: dynamic

ras486 11/17/14 3:13 PM

Deleted: 2013

817 Increasing the model resolution for the simulations is expensive however may be warranted but
818 only once we've improved source maps, included atmospheric mineral processing, and have larger
819 observational data sets to compare to.

820 In order to best match aerosol optical depth, absorbing aerosol optical depth and single
821 scattering albedo from AERONET, it is not clear that adding mineralogy improves the comparison
822 (Figure 9). Sensitivity studies with size suggest that assumed size distributions are as important as
823 the inclusion of mineralogy for correctly simulating the AERONET observations (Figure 15).
824 Similarly inclusion of mineralogy also did not significantly improve the simulation of forcing
825 efficiency compared to observations although the CAM5 mineralogy simulation with hematite
826 arising from the soil clay fraction did somewhat improve this comparison. Changes in the assumed
827 size distribution were similarly important in forcing efficiency calculations.

828 For calculating globally averaged radiative forcing, the simulations with mineral speciation
829 are as important as the assumed size distribution. The single scattering albedo of dust is likely to
830 be close to the threshold, where the sign of radiative forcing and climate response changes with
831 small changes in SSA (Perlwitz et al., 2001). In both the CAM4 and CAM5 simulations, including
832 mineralogy caused the modeled radiative forcing to switch from a small negative value (-0.05 and -
833 0.17 Wm⁻² for CAM4 and CAM5 with tuned dust) to a small positive value (+0.05 Wm⁻² for both
834 CAM4 and CAM5 with mineralogy). Notice that our results are sensitive to the poorly constrained
835 simulation of mineralogy; improvements in the simulation of mineralogy could change the
836 importance of mineralogy to aerosol properties and forcing.

837 A recent study of the radiative forcing of dust as a function of mineralogical composition
838 that does not include the spatially explicit variability of minerals estimate a TOA forcing between -
839 0.03 and -0.25 Wm⁻² from mineral dust with an internal mixture of 1.5% hematite by volume
840 (Balkanski et al., 2007). Both CAM4 and CAM5 cases with tuned dust (0.4% inclusion of hematite by
841 volume) fall within the reported range.

842 In conclusion, more work is needed to improve input mineral source maps as well as
843 mechanisms to simulate atmospheric processing. While mineralogy was not the most important

844 factor impacting the simulation of direct radiative forcing in these simulations, it was responsible
845 for increasing the radiative forcing for both models by about 0.1 Wm⁻². Mineralogy is likely to be
846 more important for soluble iron impacts on biogeochemistry (Journet et al., 2008), as well as for
847 aerosol-cloud [interactions](#) (Yin et al., 2002;Koehler et al., 2009;Hoose et al., 2008), and with this
848 paper we have constructed the speciation framework to investigate mineralogy effects on these
849 processes.

850

851 Acknowledgments:

852 [We thank Ives Balkanski for his comments and insight which improved the quality of the](#)
853 [manuscript. Also, we](#) thank the AERONET program for establishing and maintaining the used sites.
854 These simulations were conducted at the National Center for Atmospheric Research, a National
855 Science Foundation facility. N. Mahowald, R. Scanza and S. Albani would like [to](#) acknowledge the
856 support of DOE DE-SC00006735, NSF 0932946 and NSF 1003509.
857 S.Ghan and X. Liu were funded by the U.S Department of Energy Atmospheric Systems Research and
858 Climate Modeling programs. The Pacific Northwest National Laboratory (PNNL) is operated for the
859 DOE by Battelle Memorial Institute under contract DE-AC06-76RLO 1830.

860 References:

861 Albani, S., Mahowald, N., Perry, A., Scanza, R., Zender, C., Heavens, N., Maggi, V., Kok, J., and Otto-
862 Bliesner, B.: Improved dust representation in the Community Atmosphere Model, J. Adv. Model. Earth
863 Syst., doi:10.1002/2013MS000279, 2014.
864 Bagnold, R. A.: The physics of wind blown sand and desert dunes, Methuen, London, 265, 1941.
865 Balkanski, Y., Schulz, M., Claquin, T., and Guibert, S.: Reevaluation of mineral aerosol radiative forcings
866 suggests a better agreement with satellite and AERONET data, Atmos. Chem. Phys, 7, 81-95, 2007.
867 Batjes, N.: A world dataset of derived soil properties by FAO–UNESCO soil unit for global modelling, Soil
868 use and management, 13, 9-16, 1997.
869 Biscaye, P. E.: Mineralogy and sedimentation of recent deep-sea clay in the Atlantic Ocean and adjacent
870 seas and oceans, Geological Society of America Bulletin, 76, 803-832, 1965.
871 Caquineau, S., Gaudichet, A., Gomes, L., Magonthier, M. C., and Chatenet, B.: Saharan dust: Clay ratio as
872 a relevant tracer to assess the origin of soil-derived aerosols, Geophysical research letters, 25, 983-986,
873 1998.
874 Claquin, T., Schulz, M., and Balkanski, Y.: Modeling the mineralogy of atmospheric dust sources, Journal
875 of Geophysical Research, 104, 22,243-222,256, 1999.
876 Coakley Jr, J. A., Cess, R. D., and Yurevich, F. B.: The effect of tropospheric aerosols on the earth's
877 radiation budget: A parameterization for climate models, Journal of Atmospheric Sciences, 40, 116-138,
878 1983.
879 Conley, A., Lamarque, J.-F., Vitt, F., Collins, W., and Kiehl, J.: PORT, a CESM tool for the diagnosis of
880 radiative forcing, Geoscientific Model Development, 6, 469-476, 2013.
881 Cwiertny, D. M., Baltrusaitis, J., Hunter, G. J., Laskin, A., Scherer, M. M., and Grassian, V. H.:
882 Characterization and acid-mobilization study of iron-containing mineral dust source materials, Journal of
883 Geophysical Research: Atmospheres, 113, doi:10.1029/2007JD009332, 2008.

ras486 11/17/14 3:13 PM

Deleted: interactions

ras486 11/17/14 3:13 PM

Deleted: We

ras486 11/17/14 3:13 PM

Deleted: the

887 DeMott, P. J., Sassen, K., Poellot, M. R., Baumgardner, D., Rogers, D. C., Brooks, S. D., Prenni, A. J., and
 888 Kreidenweis, S. M.: African dust aerosols as atmospheric ice nuclei, *Geophysical Research Letters*, 30,
 889 1732, doi:10.1029/2003GL017410, 012003, 2003.
 890 Dubovik, O., and King, M. D.: A flexible inversion algorithm for retrieval of aerosol optical properties
 891 from Sun and sky radiance measurements, *Journal of Geophysical Research: Atmospheres* (1984–2012),
 892 105, 20673–20696, 2000.
 893 Dubovik, O., Smirnov, A., Holben, B. N., King, M. D., Kaufman, Y. J., Eck, T. F., and Slutsker, I.: Accuracy
 894 assessments of aerosol optical properties retrieved from Aerosol Robotic Network (AERONET) Sun and
 895 sky radiance measurements, *Journal of Geophysical Research*, 105, 9791–9806, 2000.
 896 Dufresne, J.-L., Gauier, C., Ricchiazzi, P., and Rouquart, Y.: Longwave Scattering Effects of Mineral
 897 Aerosols, *American Meteorological Society*, 59, 1959–1966, 2002.
 898 Fecan, F., Marticorena, B., and Bergametti, G.: Parameterization of the increase of the aeolian erosion
 899 threshold wind friction velocity due to soil moisture for arid and semi-arid areas, *Annales Geophysicae-
 900 Atmosphere Hydrospheres and Space Sciences*, 17, 149–157, 1999.
 901 Ghan, S. J., and Zaveri, R. A.: Parameterization of optical properties for hydrated internally mixed
 902 aerosol, *Journal of Geophysical Research: Atmospheres*, 112, doi:10.1029/2006JD007927, 2007.
 903 Gillette, D. A., Blifford, I. H., and Fryrear, D.: The influence of wind velocity on the size distributions of
 904 aerosols generated by the wind erosion of soils, *Journal of Geophysical Research*, 79, 4068–4075, 1974.
 905 Ginoux, P., Chin, M., Tegen, I., Prospero, J. M., Holben, B. N., Dubovik, O., and Lin, S.-J.: Sources and
 906 distribution of dust aerosols with the GOCART model, *Journal of Geophysical Research*, 106, 20255–
 907 20273, 2001.
 908 Glaccum, R. A., and Prospero, J. M.: Saharan aerosols over the tropical North Atlantic—Mineralogy,
 909 *Marine Geology*, 37, 295–321, 1980.
 910 Gomes, L., Bergametti, G., Coudé-Gaussen, G., and Rognon, P.: Submicron desert dusts: A sandblasting
 911 process, *Journal of Geophysical Research: Atmospheres* (1984–2012), 95, 13927–13935, 1990.
 912 Han, Q., Moore, J. K., Zender, C., Measures, C., and Hydes, D.: Constraining oceanic dust deposition using
 913 surface ocean dissolved Al, *Global Biogeochemical Cycles*, 22, doi:10.1029/2007GB002975, 2008.
 914 Holben, B., Eck, T., Slutsker, I., Tanre, D., Buis, J., Setzer, A., Vermote, E., Reagan, J., Kaufman, Y., and
 915 Nakajima, T.: AERONET—A federated instrument network and data archive for aerosol characterization,
 916 *Remote sensing of environment*, 66, 1–16, 1998.
 917 Holben, B. N., Tanre, D., Smirnov, A., Eck, T. F., Slutsker, I., Abuhassan, N., Newcomb, W. W., Schafer, J.
 918 S., Chatenet, B., Lavenue, F., Kaufman, Y. J., Vande Castle, J., O'Neill, N. T., Pietras, C., Pinker, R. T., Voss,
 919 K., and Zibordi, G.: An emerging ground-based aerosol climatology: Aerosol optical depth from AERONET,
 920 *Journal of Geophysical Research*, 106, 12067–12097, 2001.
 921 Hoose, C., Lohmann, U., Erdin, R., and Tegen, I.: The global influence of dust mineralogical composition
 922 on heterogeneous ice nucleation in mixed-phase clouds, *Environmental Research Letters*, 3, 025003,
 923 doi:10.1088/1748-9326/3/2/025003, 2008.
 924 Hurrell, J. W., Holland, M., Gent, P., Ghan, S., Kay, J. E., Kushner, P., Lamarque, J.-F., Large, W., Lawrence,
 925 D., and Lindsay, K.: THE COMMUNITY EARTH SYSTEM MODEL, *Bulletin of the American Meteorological
 926 Society*, 94, 1139–1360, doi:10.1175/BamS-d-12-00121.1, 2013.
 927 Hurrell, J. W., M. M. Holland, S. Ghan, J. -F. Lamarque, D. Lawrence, W. H. Lipscomb, N. Mahowald, D.
 928 Marsh, P. Rasch, D. Bader, W. D. Collins, P. R. Gent, J. J. Hack, J. Kiehl, P. Kushner, W. G. Large, S.
 929 Marshall, S. Vavrus, and Vertenstein, M.: The Community Earth System Model: A Framework for
 930 Collaborative Research, *Bulletin of the American Meteorological Society*, 94, 1139–1360,
 931 doi:10.1175/BAMS-D-12-00121.1, 2014.
 932 Iacono, M. J., Delamere, J. S., Mlawer, E. J., Shephard, M. W., Clough, S. A., and Collins, W. D.: Radiative
 933 forcing by long-lived greenhouse gases: Calculations with the AER radiative transfer models, *Journal of
 934 Geophysical Research: Atmospheres*, 113, D13103, doi:10.1029/2008JD009944, 2008.
 935 IPCC: Summary for Policymakers, in: *Climate Change 2007: The Physical Science Basis. Contribution of
 936 Working Group I to the Fourth Assessment Report of the Intergovernmental Panel on Climate Change*,

937 edited by: Solomon, S., Qin, D., Manning, M., Chen, Z., Marquis, M., Averyt, K., Tignor, M., and Miller, H.
 938 L., Cambridge University Press, Cambridge, UK and New York, NY, USA, 2007.
 939 Jickells, T., An, Z., Andersen, K., Baker, A., Bergametti, G., Brooks, N., Cao, J., Boyd, P., Duce, R., Hunter,
 940 K., Kawahata, H., Kubilay, N., laRoche, J., Liss, P., Mahowald, N., Prospero, J., Ridgwell, A., Tegen, I., and
 941 Torres, R.: Global iron connections between dust, ocean biogeochemistry and climate, *Science*, 308, 67-
 942 71, 2005.
 943 Joseph, J., Wiscombe, W., and Weinman, J.: The delta-Eddington approximation for radiative flux
 944 transfer, *Journal of the Atmospheric Sciences*, 33, 2452-2459, 1976.
 945 Journet, E., Desbouefs, K., Caquineau, S., and Colin, J.-L.: Mineralogy as a critical factor of dust iron
 946 solubility, *Geophysical Research Letters*, 35, L07805, doi:10.1029/2007GL031589, 2008.
 947 Journet, E., Balkanski, Y., and Harrison, S.: A new data set of soil mineralogy for dust-cycle modeling,
 948 *Atmospheric Chemistry and Physics*, 14, 3801-3816, doi:10.5194/acp-14-3801-2014, 2014.
 949 Kalashnikova, O., and Kahn, R. A.: Mineral dust plume evolution over the Atlantic from MISR and MODIS
 950 aerosol retrievals, *Journal of Geophysical Research*, 113, D24204, doi:10.1029/2008JD010083, 2008.
 951 Kandler, K., Schütz, L., Deutscher, C., Ebert, M., Hofmann, H., Jäckel, S., Jaenicke, R., Knippertz, P., Lieke,
 952 K., and Massling, A.: Size distribution, mass concentration, chemical and mineralogical composition and
 953 derived optical parameters of the boundary layer aerosol at Tinfou, Morocco, during SAMUM 2006,
 954 *Tellus B*, 61, 32-50, 2009.
 955 Karydis, V., Kumar, P., Barahona, D., Sokolik, I., and Nenes, A.: On the effect of dust particles on global
 956 cloud condensation nuclei and cloud droplet number, *Journal of Geophysical Research: Atmospheres*,
 957 116, D23204, doi:10.1029/2011JD016283, 2011.
 958 Kiefert, L., McTainsh, G., and Nickling, W.: Sedimentological characteristics of Saharan and Australian
 959 dusts, in: *The impact of desert dust across the Mediterranean*, Springer, the Netherlands, 183-190,
 960 1996.
 961 Koehler, K. A., Kreidenweis, S. M., DeMott, P. J., Petters, M. D., Prenni, A. J., and Carrico, C. M.:
 962 Hygroscopicity and cloud droplet activation of mineral dust aerosol, *Geophysical Research Letters*, 36,
 963 L08805, doi:10.1029/2009GL037348, 2009.
 964 Kok, J.: A scaling theory for the size distribution of emitted dust aerosols suggests climate models
 965 underestimate the size of the global dust cycle, *Proceedings of the National Academy of Science USA*,
 966 108, 1016-1021, 2011.
 967 Kok, J. F., Parteli, E. J., Michaels, T. I., and Karam, D. B.: The physics of wind-blown sand and dust,
 968 *Reports on Progress in Physics*, 75, 106901, doi:10.1088/0034-4885/75/10/106901, 2012.
 969 Kolmogorov, A. N.: On the logarithmically normal law of distribution of the size of particles under
 970 pulverisation, *Doklady Akademii Nauk SSSR*, 31, 99-101, 1941.
 971 Lamarque, J.-F., Emmons, L., Hess, P., Kinnison, D. E., Tilmes, S., Vitt, F., Heald, C., Holland, E. A.,
 972 Lauritzen, P., and Neu, J.: CAM-chem: description and evaluation of interactive atmospheric chemistry in
 973 the Community Earth System Model, *Geoscientific Model Development*, 5, 369-411, 2012.
 974 Lancaster, N., and Baas, A.: Influence of vegetation cover on sand transport by wind: field studies at
 975 Owens Lake, California, *Earth Surface Processes and Landforms*, 23, 69-82, 1998.
 976 Levin, Z., Teller, A., Ganor, E., and Yin, Y.: On the interactions of mineral dust, sea-salt particles, and
 977 clouds: A measurement and modeling study from the Mediterranean Israeli Dust Experiment campaign,
 978 *Journal of geophysical research*, 110, D20202, doi:10.1029/2005JD005810, 2005.
 979 Li, F., Vogelmann, A., and Ramanathan, V.: Saharan dust aerosol radiative forcing measured from space,
 980 *Journal of Climate*, 17, 2558-2571, 2004.
 981 Liu, X., Easter, R. C., Ghan, S. J., Zaveri, R., Rasch, P., Shi, X., Lamarque, J.-F., Gettelman, A., Morrison, H.,
 982 and Vitt, F.: Toward a minimal representation of aerosols in climate models: Description and evaluation
 983 in the Community Atmosphere Model CAM5, *Geoscientific Model Development*, 5, 709-739, 2012.
 984 Mahowald, N., and Kiehl, L.: Mineral aerosol and cloud interactions, *Geophysical Research Letters*, 30,
 985 1475, doi:10.1029/2002GL016762, 2003.

986 Mahowald, N., D. Muhs, Levis, S., Rasch, P., Yoshioka, M., and Zender, C.: Change in atmospheric mineral
 987 aerosols in response to climate: last glacial period, pre-industrial, modern and doubled-carbon dioxide
 988 climates *Journal of Geophysical Research*, 111, D10202, doi:10.1029/2005JD006653, 2006.
 989 Mahowald, N., Kloster, S., Engelstaedter, S., Moore, J. K., Mukhopadhyay, S., McConnell, Albani, S.,
 990 Doney, S., Bhattacharya, A., Curran, M., Flanner, M., Hoffman, F., Lawrence, D., Lindsay, K., Mayewski,
 991 P., Neff, J., Rothenberg, D., Thomas, E., Thornton, P., and Zender, C.: Observed 20th century desert dust
 992 variability: impact on climate and biogeochemistry, *Atmospheric Chemistry and Physics*, 10, 10875-
 993 10893, 2010.
 994 Martin, J., Gordon, R. M., and Fitzwater, S. E.: The case for iron, *Limnology and Oceanography*, 36, 1793-
 995 1802, 1991.
 996 Miller, R., Tegen, I., and Perlwitz, J.: Surface radiative forcing by soil dust aerosols and the hydrologic
 997 cycle, *Journal of Geophysical Research*, 109, D04203, doi:10.1029/2003JD004085, 2004.
 998 Miller, R., Cakmur, R., Perlwitz, J., Geogdzhayev, I., Ginoux, P., Kohfeld, K., Koch, D., Prigent, C., Ruedy,
 999 R., Schmidt, G., and Tegen, I.: Mineral dust aerosols in the NASA Goddard Institute of Space Sciences
 1000 ModelE Atmospheric General Circulation Model, *Journal of Geophysical Research*, 111, D06208,
 1001 doi:10.1029/2005JD005796, 2006.
 1002 Miller, R. L., and Tegen, I.: Climate Response to Soil Dust Aerosols, *Journal of Climate*, 11, 3247-3267,
 1003 1998.
 1004 Moosmüller, H., Engelbrecht, J. P., Skiba, M., Frey, G., Chakrabarty, R. K., and Arnott, W. P.: Single
 1005 scattering albedo of fine mineral dust aerosols controlled by iron concentration, *Journal of Geophysical*
 1006 *Research: Atmospheres*, 117, D11210, doi:10.1029/2011JD016909, 2012.
 1007 Nickovic, S., Vukovic, A., Vujadinovic, M., Djurdjevic, V., and Pejanovic, G.: Technical Note: High-
 1008 resolution mineralogical database of dust-productive soils for atmospheric dust modeling, *Atmos. Chem.*
 1009 *Phys*, 12, 845-855, 2012.
 1010 Niklasson, G. A., Granqvist, C., and Hunderi, O.: Effective medium models for the optical properties of
 1011 inhomogenous materials, *Appl. Optics*, 20, 26-30, doi:10.1364/AO.20.000026, 1981.
 1012 Okin, G.: A new model of wind erosion in the presence of vegetation, *Journal of Geophysical Research-*
 1013 *Earth Surface*, 113, F02S10, doi:10.1029/2007JF000758, 2008.
 1014 Patadia, F., Yang, E.-S., and Christopher, S.: Does dust change the clear sky top of atmosphere shortwave
 1015 flux over high surface reflectance regions?, *Geophysical Research Letters*, 36, L15825,
 1016 doi:10.1029/2009GL039092, 2009.
 1017 Perlwitz, J., Tegen, I., and Miller, R.: Interactive soil dust aerosol model in the GISS GCM 1. Sensitivity of
 1018 the soil dust cycle to radiative properties of soil dust aerosols, *Journal of Geophysical Research*, 106,
 1019 18,167-118,192, 2001.
 1020 Rasch, P. J., Feichter, H., Law, K., Mahowald, N., Penner, J., Benkovitz, C., Genthon, C., Giannakopoulos,
 1021 C., Kasibhatla, P., Koch, D., Levy, H., Maki, T., Prather, M., Roberts, D. L., Roelofs, G.-J., Stevenson, D.,
 1022 Stockwell, Z., Taguchi, S., Chipperfield, M., Baldocchi, D., McMurry, P., Barrie, L., Balkanski, Y., Chatfield,
 1023 B., Jacob, D., Kritz, M., Lawrence, M., Lee, H. N., Leaitch, R., Lelieveld, J., Noone, K. J., Seinfeld, J.,
 1024 Stenchikov, G., Schwarz, S., Walcek, C., and Williamson, D.: An Assessment of Scavenging and Deposition
 1025 Processes in Global Models: Results from the WCRP Cambridge Workshop of 1995, *Tellus*, 52B, 1025-
 1026 1056, 2000.
 1027 Reid, E., Reid, J., Meier, M., Dunlap, M., Cliff, S., Broumas, A., Perry, K., and Maring, H.: Characterization
 1028 of African dust transported to Puerto Rico by individual particle and size segregated bulk analysis, *JGR-*
 1029 *Atmospheres*, 108, 8591, doi:10.1029/2002JD002935, 2003.
 1030 Sabre, M., Lopez, M., Alfaro, S., Rajot, J., and Gomes, L.: Characterization of the fine dust particle
 1031 production process by wind erosion for two types of bare soil surfaces, *Proceedings of Wind Erosion: An*
 1032 *International Symposium/Workshop*, 3-5 June 1997, Manhattan, Kansas, USA, 1997.
 1033 Schulz, M., Balkanski, Y. J., Guelle, W., and Dulac, F.: Role of aerosol size distribution and source location
 1034 in a three-dimensional simulation of a Saharan dust episode tested against satellite-derived optical
 1035 thickness, *Journal of Geophysical Research*, 103, 10579-10592, 1998.

1036 Seinfeld, J., and Pandis, S.: Atmospheric Chemistry and Physics, John Wiley and Sons, Inc, New York,
1037 1326 pp., 1998.

1038 Shao, Y., Raupach, M., and Findlater, P.: Effect of saltation bombardment on the entrainment of dust by
1039 wind, *Journal of Geophysical Research: Atmospheres* (1984–2012), 98, 12719-12726, 1993.

1040 Shen, Z., Li, X., Cao, J., Caquineau, S., Wang, Y., and Zhang, X.: Characteristics of clay minerals in Asian
1041 dust and their environmental significance, *China Particuology*, 3, 260-264, 2005.

1042 Shi, Z., Shao, L., Jones, T., and Lu, S.: Microscopy and mineralogy of airborne particles collected during
1043 severe dust storm episodes in Beijing, China, *Journal of Geophysical Research: Atmospheres*, 110,
1044 D01303, doi:10.1029/2004JD005073, 2005.

1045 Siegel, D. A., and Deuser, W. G.: Trajectories of sinking particles in the Sargasso Sea: modeling of
1046 statistical funnels above deep-ocean sediment traps, *Deep-Sea Research*, 44, 1519-1541, 1997.

1047 Sokolik, I. N., and Toon, O. B.: Incorporation of mineralogical composition into models of the radiative
1048 properties of mineral aerosol from UV to IR wavelengths, *Journal of Geophysical Research*, 104, 9423-
1049 9444, 1999.

1050 Suarez, M. J., Rienecker, M., Todling, R., Bacmeister, J., Takacs, L., Liu, H., Gu, W., Sienkiewicz, M.,
1051 Koster, R., and Gelaro, R.: The GEOS-5 Data Assimilation System-Documentation of Versions 5.0. 1, 5.1.
1052 0, and 5.2. 0, <http://nttrs.nasa.gov/archive/nasa/casi.ntrs.nasa.gov/20120011955.pdf> (last access: 30
1053 June 2014), 2008.

1054 Swap, R., Garstang, M., Greco, S., Talbot, R., and Kallberg, P.: Saharan dust in the Amazon Basin, *Tellus*,
1055 44B, 133-149, 1992.

1056 Wang, H., Easter, R., Rasch, P., Wang, M., Liu, X., Ghan, S., Qian, Y., Yoon, J.-H., Ma, P.-L., and Velu, V.:
1057 Sensitivity of remote aerosol distributions to representation of cloud-aerosol interactions in a global
1058 climate model, *Geoscientific Model Development*, 6, 765-782, doi:10.5194/gmd-6-765-2013, 2013.

1059 Wiscombe, W. J.: Improved Mie scattering algorithms, *Applied optics*, 19, 1505-1509, 1980.

1060 Woodward, S.: Modeling the atmospheric life cycle and radiative impact of mineral dust in the Hadley
1061 Centre climate model, *JGR*, 106, 18155-118166, 2001.

1062 Yin, Y., Wurzler, S., Levin, Z., and Reisin, T. G.: Interactions of mineral dust particles and clouds: Effects
1063 on precipitation and cloud optical properties, *Journal of Geophysical Research: Atmospheres*, 107, AAC
1064 191-AAC, 19-14, doi:10.1029/2001JD001544, 2002.

1065 Yoshioka, M., Mahowald, N., Conley, A., Collins, W., Fillmore, D., and Coleman, D.: Impact of desert dust
1066 radiative forcing on Sahel precipitation: relative importance of dust compared to sea surface
1067 temperature variations, vegetation changes and greenhouse gas warming, *Journal of Climate*, 20, 1445-
1068 1467, 2007.

1069 Zender, C., Bian, H., and Newman, D.: Mineral Dust Entrainment and Deposition (DEAD) model:
1070 Description and 1990s dust climatology, *Journal of Geophysical Research*, 108, 4416,
1071 doi:10.1029/2002JD002775, 2003.

1072 Zhang, J., and Christopher, S.: Long wave radiative forcing of Saharan dust aerosols estimated from
1073 MODIS, MISR and CERES observations on TERRA, *Geophysical Research Letters*, 30, 2188,
1074 doi:10.1029/2003GL018479, 2003.

1075 Zhang, Y., Scanza, R., Mahowald, N., and Journet, E.: Modeling the Global Emission, Transport and
1076 Deposition of Trace Elements associated with Mineral Dust, in preparation, 2014.

1077
1078
1079
1080
1081

1082
1083
1084
1085
1086
1087
1088
1089
1090
1091
1092
1093
1094
1095
1096
1097
1098
1099
1100
1101
1102

1103 **Tables**

1104
1105
1106
1107
1108
1109

Table 1: Mean Mineralogical Table from Claquin et al. 1999. Gypsic xerosols and yermosols (Xy,Yy), Gleyic Solontchaks (Zg), and Orthic Solontchaks (Zo), and salt flats (ST) are renormalized to 100. Hematite is added to the clay fraction by subtracting the mass from illite following Balkanski et al., 2007 and Nickovic et al., 2011. For the sensitivity study involved in only a clay fraction source of hematite, the minerals with silt sized source fractions were equally scaled from the mass removed from hematite.

1110
1111
1112
1113
1114
1115

ras486 11/17/14 3:13 PM
Deleted: ... [1]

Soil Types	Clay Fraction						Silt Fraction				
	Ill	Kaol	Sme	Cal	Quar	Hem	Quar	Feld	Cal	Hem	Gyp
I	39	20	29	4	7	1	52	40	6	1	1
Jc	22	9	46	11	12	0	30	38	29	0	2
Je	17	23	55	1	3	1	86	10	2	1	1
Qa	20	54	21	0	4	1	83	15	0	1	1
Qc	12	67	5	1	11	4	80	14	1	4	1
Qf	22	48	23	1	5	1	82	15	1	1	1
Ql	3	77	3	1	9	7	69	22	1	7	1
Rc	39	39	9	4	7	3	74	19	3	3	1
Re	30	52	10	1	5	2	58	38	1	2	1
So	35	32	17	6	7	2	70	23	4	2	1
Vc	12	27	48	4	5	4	31	61	3	4	1
Xh	18	54	22	1	3	2	72	24	1	2	1
Xk,Yk	55	13	16	11	3	2	76	7	14	2	1
Xl,Yl	43	20	20	7	7	2	69	23	5	2	1
Xt	20	50	21	3	5	1	16	78	4	1	1
Xy,Yy	27	18	40	8	7	0	54	25	15	0	6
Zg	16	33	24	21	5	0	45	25	18	0	13
Zo	30	6	46	11	7	1	32	41	21	1	6
Zt	25	33	25	10	6	0	22	65	12	0	1
SD	49	9	26	1	14	1	91	6	1	1	1
ST	39	4	26	29	1	1	4	1	74	1	21

1116
1117
1118
1119
1120
1121
1122
1123
1124
1125
1126
1127
1128
1129
1130

1133 **Table 2a:** The fraction of dust aerosol mass contributed by the soil clay and silt fractions for each of the
1134 4 particle size bins for the bulk aerosol scheme in CAM4 from work by Kok, 2011.
1135

Particle Size Bin	Lower bin limit D_p (μm)	Upper bin limit D_p (μm)	Fraction of aerosol mass from soil clay fraction	Fraction of aerosol mass from soil silt fraction
1	0.1	1	1	0
2	1	2.5	0.970	0.030
3	2.5	5	0.625	0.375
4	5	10	0.429	0.571

1136

1137 **Table 2b:** The fraction of dust aerosol mass contributed by the soil clay and silt fractions for each of the
1138 2 particle modes for the modal aerosol scheme in CAM5 from work by Kok, 2011.
1139

Particle Mode	Lower bin limit D_p (μm)	Upper bin limit D_p (μm)	Fraction of aerosol mass from soil clay fraction	Fraction of aerosol mass from soil silt fraction
1	0.1	1	1	0
2	1	10	0.695	0.305

1140

1141

1142

1143

1144

1145

1146

1147

1148

1149

1150

1151

1152

1153

1154

1155
1156
1157
1158
1159
1160
1161

1162

1163

1164

1165

1166

1167

1168

1169

1170

1171

1172

1173

1174

1175

1176

1177

Table 3: Refractive indices of minerals used, wavelengths of refractive indices and references for input into CAM4 and CAM5. Refractive indices specified as ‘Zender’ are a Maxwell-Garnet internal mixture of 48% quartz, 25% illite, 25% montmorillonite and 2% calcite by volume. These were used primarily to simplify the comparison between CAM4 and CAM5. Longwave optics from CAM3 (Mahowald et al., 2006) were substituted for CAM4 as a solver was not available to calculate the LW absorption coefficients from the refractive indices.

Minerals	Refractive Indices	Wavelengths	CAM4	CAM5
Illite	Egan and Hilgeman 1979	0.19 to 2.5 μm	X	X
	Querry 1987	2.5 to 50.0 μm	X	X
Kaolinite	Egan and Hilgeman 1979	0.19 to 2.5 μm	X	X
	Querry 1987	2.5 to 50.0 μm	X	X
Montmorillonite	Egan and Hilgeman 1979	0.19 to 2.5 μm	X	X
	Querry 1987	2.5 to 50.0 μm	X	X
Quartz	Zender	0.2 to 40.0 μm	X	
Calcite	Zender	0.2 to 40.0 μm	X	
Hematite	A.H.M.J. Triaud	0.1 to 40.7 μm	X	X
Feldspar	Zender	0.2 to 40.0 μm	X	
Gypsum	Zender	0.2 to 40.0 μm	X	
Dust-Other	Zender	0.2 to 40.0 μm		X

1178
1179
1180
1181
1182
1183
1184
1185
1186
1187

1188
1189
1190
1191
1192
1193
1194
1195
1196
1197
1198
1199
1200
1201

1202

1203

1204 **Table 5:** Observations of mineralogy used to evaluate simulated mineral distributions in CAM4 and
1205 CAM5. Near-surface observational data was chosen in order to compare to near-surface mineral
1206 concentrations in the models. Ocean core sediment data is compared to bulk dry and wet deposition

1207

Reference	Location	Type of Data	Month	Type
Biscaye 1965	Atlantic Ocean	Sediment	N/A	K/I
Cacqueineau et al. 1998	Tropical N. Atlantic	Suspended (< 20 m) Ratio	April	K/I
Falkovich et al. 2001	Israel	Suspended (< 20 m) Ratio	March	K/I; C/Q; F/Q
Glaccum and Prospero 1980	Tropical N. Atlantic	Suspended (< 20 m) Ratio	Aug.	K/I; C/Q; F/Q
Kandler et al. 2009	Morocco	Suspended (< 20 m) Ratio, Volume Fraction	May	K/I; H/I; C/Q; F/Q; H/Q; I,K,Q,C,H,F,G
Kiefert et al. 1996	Charleville, AUS	Suspended (< 20 m) Ratio	Dec.	K/I
Prospero and Bonatti 1969	Equitorial Pacific	Suspended (< 20 m) Ratio	FMA	K/I; F/Q
Shen et al. 2005	N. China	Suspended (< 20 m) Ratio	MAM	K/I
Shi et al. 2005	Beijing	Suspended (< 20 m) Ratio	March	C/Q; F/Q; H/Q

ras486 11/17/14 3:13 PM

Deleted: Isreal

1208

1209

1210

1211

1212

1213

1214

1215

1216

1217

1218

1219

1220

1222
1223
1224
1225
1226
1227
1228
1229

1230

Table 6a: The mean and standard deviation for annually averaged AERONET (Holben et al., 1998,2001) retrievals and the annually averaged means for CAM4 with untuned (default) dust (CAM4-d), with tuned dust (CAM4-t) and with mineralogy (CAM4-m), for CAM5 with untuned dust (CAM5-d), with tuned dust (CAM5-t) and with mineralogy (CAM5-m) for Aerosol Optical Depth (AOD), Absorbing AOD, and Single Scattering Albedo (SSA) at 533nm at AERONET sites where $AOD_{dust} > 0.5 * AOD_{total}$. The lower portion of the table lists the means for the sensitivity studies for CAM4 and CAM5 with tuned dust and release (default) size distribution (CAM4-trs, CAM5-trs) and for CAM4 and CAM5 mineralogy simulations with the source of hematite coming solely from the soil clay fraction (CAM4-mH, CAM5-mH).

	AOD	AAOD	SSA
AERONET	0.383	0.046	0.923
std	0.115	0.011	0.013
CAM4-d	0.288	0.037	0.885
CAM4-t	0.214	0.015	0.935
CAM4-m	0.210	0.009	0.958
CAM5-d	0.274	0.037	0.887
CAM5-t	0.350	0.026	0.933
CAM5-m	0.329	0.042	0.890
CAM4-trs	0.267	0.015	0.948
CAM4-mH	0.211	0.009	0.959
CAM5-trs	0.423	0.028	0.941
CAM5-mH	0.330	0.038	0.901

1231

1232
1233
1234
1235
1236

1237

Table 6b: The standard deviation in the model over the standard deviation in AERONET. Values less than 1 indicate that the model is not capturing the dynamic range from the observations while values greater than 1 indicate the model is simulating a larger range than observed. This metric is used to test whether the simulations with mineralogy are better capturing the range in the observations, with red denoting an increase in ability and blue signifying a decrease.

	AOD	AAOD	SSA
CAM4-d	0.58	0.56	0.79
CAM4-t	0.50	0.31	0.59
CAM4-m	0.49	0.16	0.57
CAM5-d	0.75	1.13	1.03
CAM5-t	1.00	0.80	0.70
CAM5-m	0.93	1.40	1.10
CAM4-trs	0.66	0.31	0.51
CAM4-mH	0.49	0.16	0.57
CAM5-trs	1.20	0.84	0.62
CAM5-mH	0.94	1.25	0.98

1238

Table 7: Comparison of observed top of atmosphere clear-sky radiative forcing efficiencies (RFE) ($\text{Wm}^{-2}\text{r}^{-1}$) over N. Atlantic and N. Africa regions with simulated RFE. Simulations are for CAM4 and CAM5 with release dust, tuned dust and mineralogy in the upper portion of the table. The sensitivity studies with tuned dust and release size distribution, and with the source of hematite coming solely from the soil clay fraction for CAM4 and CAM5 comprise the lower portion of the table.

Reference; domain	Li et. al. 2004; 15- 25 N, 45-15 W	Li et. al. 2004; 15- 25 N, 45-15 W	Zhang and Christopher 2004; 15-35N,18W-40E	Patadia et. al. 2009; 15- 30N,30E-10W
Observed	TOA:SW (JJA) -35 ± 3	TOA:SW (NDJ) -26 ± 3	TOA:LW (Sept.) 15	TOA:SW (JJA) 0 (albedo = 0.4)
CAM4-d	-25.2	-30.6	0.0	18.1
CAM4-t	-34.1	-36.2	9.5	3.8
CAM4-m	-25.3	-25.9	9.9	11.6
CAM5-d	-19.7	-22.0	4.4	21.9
CAM5-t	-31.2	-31.0	6.7	-1.3
CAM5-m	-23.4	-23.9	5.6	10.0
CAM4-trs	-32.4	-33.3	7.4	-1.5
CAM5-trs	-32.0	-31.7	5.8	-3.8
CAM4-mH	-25.4	-25.9	9.9	11.4
CAM5-mH	-25.7	-25.8	5.7	5.9

1262 **Table 8a:** Simulated annual average global all-sky radiative forcing.

1263

Model	AOD	TOA	TOAsw	TOAlw	ATM	ATMsw	ATMlw	SFC	SFCsw	SFClw
CAM4-d	0.029	0.08	0.08	0	1.59	1.59	0	-1.51	-1.51	0
CAM4-t	0.015	-0.05	-0.14	0.09	0.23	0.56	-0.33	-0.28	-0.7	0.42
CAM4-m	0.015	0.05	-0.04	0.09	0.23	0.56	-0.33	-0.18	-0.6	0.42
CAM5-d	0.023	0.17	0.09	0.08	0.96	1.33	-0.37	-0.8	-1.25	0.45
CAM5-t	0.033	-0.17	-0.33	0.16	0.22	0.77	-0.55	-0.39	-1.1	0.71
CAM5-m	0.031	0.05	-0.08	0.13	0.67	1.17	-0.5	-0.62	-1.25	0.63
CAM4-trs	0.021	-0.15	-0.24	0.09	0.24	0.57	-0.33	-0.38	-0.8	0.42
CAM4-mH	0.015	0.05	-0.04	0.09	0.23	0.56	-0.33	-0.18	-0.6	0.42
CAM5-trs	0.042	-0.29	-0.47	0.17	0.25	0.83	-0.57	-0.55	-1.29	0.75
CAM5-mH	0.032	-0.04	-0.15	0.12	0.58	1.07	-0.48	-0.62	-1.22	0.60

1264

1265 **Table 8b:** Simulated regional annual average global all-sky radiative forcing.

1266

	Model	TOA	TOAsw	TOAlw	ATM	ATMsw	ATMlw	SFC	SFCsw	SFClw	AOD
N. Atlantic; 0°-30°N, 50°-20°W	CAM4-t	-0.39	-0.54	0.15	1.24	1.60	-0.36	-1.62	-2.14	0.51	0.05
	CAM4-m	-0.13	-0.28	0.16	1.14	1.50	-0.36	-1.27	-1.78	0.52	0.05
	CAM5-t	-0.39	-0.56	0.16	0.76	1.07	-0.30	-1.16	-1.63	0.47	0.04
	CAM5-m	0.09	-0.04	0.13	1.57	1.83	-0.26	-1.48	-1.86	0.38	0.04
N. Africa; 5°- 35°N, 18°W- 40°E	CAM4-t	-0.12	-1.38	1.26	2.14	8.10	-5.96	-2.26	-9.48	7.22	0.21
	CAM4-m	1.30	0.02	1.29	2.28	8.28	-6.00	-0.98	-8.26	7.28	0.20
	CAM5-t	-1.10	-2.90	1.81	1.61	9.82	-8.21	-2.71	-12.73	10.02	0.36
	CAM5m	1.48	0.02	1.46	7.15	14.57	-7.42	-5.68	-14.56	8.88	0.34
W. Indian Ocean; 10°S- 15°N, 50°-70°E	CAM4-t	-0.88	-1.42	0.54	1.35	3.27	-1.92	-2.23	-4.69	2.47	0.10
	CAM4-m	-0.21	-0.76	0.55	1.31	3.25	-1.93	-1.52	-4.00	2.49	0.09
	CAM5-t	-1.65	-2.45	0.79	1.27	4.09	-2.82	-2.93	-6.54	3.61	0.18
	CAM5-m	-0.48	-1.12	0.64	3.83	6.38	-2.54	-4.31	-7.50	3.18	0.17

1267

1268

1269

1270

1271

1272

1273

1274 **Table 9:** Percent Change in annual all-sky radiative forcing for CAM4 and CAM5 from default to tuned
1275 dust (C4:d-t, C5:d-t), tuned dust to tuned dust plus release size distribution (C4:t-trs, C5:t-trs), and tuned
1276 dust to mineralogy (C4:t-m, C5:t-m).

1277

% change	TOA	TOAsw	TOAlw	ATM	ATMsw	ATMlw	SFC	SFCsw	SFClw
C4:d-t	-162.5%	-275.0%	N/A	-85.5%	-64.8%	N/A	-81.5%	-53.6%	N/A
C4:t-trs	200.0%	71.4%	0.0%	4.3%	1.8%	0.0%	35.7%	14.3%	0.0%
C4:t-m	-200.0%	-71.4%	0.0%	0.0%	0.0%	0.0%	-35.7%	-14.3%	0.0%
C5:d-t	-200.0%	-466.7%	100.0%	-77.1%	-42.1%	48.6%	-51.3%	-12.0%	57.8%
C5:t-trs	70.6%	42.4%	6.3%	13.6%	7.8%	3.6%	41.0%	17.3%	5.6%
C5:t-m	-129.4%	-75.8%	-18.8%	204.5%	51.9%	-9.1%	59.0%	13.6%	-11.3%

1278

1279

1280

1281 **Table S1:** Atmospheric loading, total deposition, and emission (Tg) of the minerals for CAM4-m.

	Load	Dep.	Em.
Illite	4.2	372.8	370.1
Kaolinite	2.2	193.8	192.3
Montmorillonite	2.8	248	246.2
Quartz	4.1	572.8	568.9
Calcite	1.3	146.2	145.1
Hematite	0.2	24.2	24
Feldspar	1.4	206.3	205
Gypsum	0.1	15.4	15.3

1282

1283

1284

1285

1286

1287

1288

1289

1290

1291

1292

1293
1294
1295
1296
1297
1298
1299
1300

1301 **Figure Captions**

1302 **Figure 1.** Mineral maps for CAM4 and AM5 based on work by Claquin et al. (1999) and Nicovic et al.
1303 (2011). Illite (a), Kaolinite (b), Montmorillonite (c) are clay-sized (0-2 μ m). Hematite (d) has the same
1304 distribution for both clay-sized and silt-sized (2-20 μ m). Quartz (e), Calcite (f), Feldspar (g), Gypsum (h)
1305 and Other-coarse (i) silt-sized. CAM4 includes Illite (a), Kaolinite (b), Montmorillonite (c), Hematite (d),
1306 Quartz (e), Calcite (f), Feldspar (g), and Gypsum (h). CAM5 includes Illite (a), Kaolinite (b),
1307 Montmorillonite (c), Hematite (d) and Other-Coarse (i) which represents quartz, calcite, feldspar, and
1308 gypsum.

1309
1310 **Figure 2.** Total percent column mineral distributions for CAM4 shown as the sum of all four bins for
1311 each mineral. Hematite (f) and Gypsum (h) are scaled by 10 so that they can be visually compared with
1312 Illite (a), Kaolinite (b), Montmorillonite (c), Quartz (d), Calcite (e) and Feldspar (g).

1313
1314 **Figure 3.** Total percent column mineral distributions for CAM5 shown as the sum of the fine mode
1315 (mode 1) and coarse mode (mode 3) for each mineral. Hematite (d) is scaled by 10 so that it can be
1316 visually compared with Illite (a), Kaolinite (b) and Montmorillonite (c).

1317
1318 **Figure 4.** Relative mass abundance of minerals near the surface as modeled compared to observations
1319 from Kandler et al. (2009) for CAM4, bins 1-4, and CAM5, mode 1 and mode 3. The month of May was
1320 averaged from 2006-2011 for the models. The CAM4 comparison is for Quartz (c), Calcite (d), Feldspar
1321 (f) and Gypsum (g). Comparisons for CAM4 and CAM5 include Illite (a), Kaolinite (b) and Hematite (e).

1322
1323 **Figure 5.** Kaolinite/Illite mineral ratio of mineral concentrations near the surface from CAM4 and CAM5
1324 (kg K/ kg I) compared to bulk observational ratios (kg K/ kg I) from field work by Shen et al. (2005),
1325 Glaccum and Prospero (1980), Prospero and Bonatti (1969), Caquineau et al. (1998), Kiefert et al. (1996)
1326 and Falkovich et al. (2001). Colored values in (c) represent averages for the month in which the
1327 observations occurred while the grey symbols represent daily averaged values over the course of the
1328 simulations (2006-2011).

1329
1330 **Figure 6.** Calcite, Feldspar / Quartz mineral ratio comparison of mineral concentrations near the surface
1331 from CAM4 (e.g. kg C/ kg Q) to bulk observational ratios from field work by Glaccum and Prospero
1332 (1980), Prospero and Bonatti (1969), Kiefert et al. (1996) Falkovich et al. (2001) and Shi et al. (2005).
1333 Bright blue and red symbols in (c) represent averages for the month in which the observations occurred
1334 while the pale red and blue symbols represent daily averaged values over the course of the simulations
1335 (2006-2011).

1336
1337
1338
1339
1340
1341
1342
1343
1344
1345
1346
1347
1348
1349
1350
1351
1352
1353
1354
1355
1356
1357
1358
1359
1360
1361
1362
1363
1364
1365
1366
1367
1368
1369
1370
1371
1372
1373
1374
1375
1376
1377
1378
1379
1380
1381

1382

1383

1384

Figure 7: Kaolinite/Illite mineral ratio of wet and dry deposition for bin 1 and bin 2 from CAM4 (a) (kg K/kg I) and from characteristic basal X-ray diffraction maxima ratios of K/I of ocean core sediments (b) (Biscaye 1965). Data is segregated by latitude bands in scatterplot (c).

Figure 8: Kaolinite/Illite mineral ratio of wet and dry deposition for mode 1 from CAM5 (a) (kg K/kg I) and from characteristic basal X-ray diffraction maxima ratios of K/I of ocean core sediments (b) (Biscaye 1965). Data is segregated by latitude bands in scatterplot (c).

Figure 9: Annually averaged modeled Aerosol Optical Depth (a,b), Absorbing Aerosol Optical Depth (c,d) and Single Scattering albedo (e,f) at 533nm compared to annually averaged AERONET retrievals at sites where modeled $AOD_{dust} > AOD_{total} * 0.5$. CAM4 (a,c,e) and CAM5 (b,d,f) are shown.

Figure 10: Model Single Scattering Albedo at gridcells with $AOD_{dust} > 0.5 * AOD_{total}$ in CAM4 mineralogy is compared to total percent column hematite (a) and total percent column black carbon (b). The location of AERONET sites used in the comparison in Figure 9 are plotted in blue.

Figure 11: Model Single Scattering Albedo from CAM5 with mineralogy is compared to total percent column hematite (a) and total percent column black carbon (b). The location of AERONET sites used in the comparison in Figure 9 are plotted in blue.

Figure 12. Spatial distribution of annual all-sky radiative forcing (SW+LW) at the surface for CAM4 with tuned dust and with mineralogy (a,c) and for CAM5 with tuned dust and mineralogy (b,d).

Figure 13. Spatial distribution of annual all-sky radiative forcing (SW+LW) in the atmosphere for CAM4 with tuned dust and with mineralogy (a,c) and for CAM5 with tuned dust and mineralogy (b,d).

Figure 14. Spatial distribution of annual all-sky radiative forcing (SW+LW) at the top of atmosphere for CAM4 with tuned dust and with mineralogy (a,c) and for CAM5 with tuned dust and mineralogy (b,d).

Figure 15: Annually averaged modeled Aerosol Optical Depth (a,b), Absorbing Aerosol Optical Depth (c,d) and Single Scattering albedo (e,f) compared to annually averaged AERONET retrievals at 533nm at sites where modeled $AOD_{dust} > AOD_{total} * 0.5$. CAM4 (a,c,e) and CAM5 (b,d,f) are shown for tuned dust, mineralogy, tuned dust + release size and mineralogy with hematite in soil clay only.

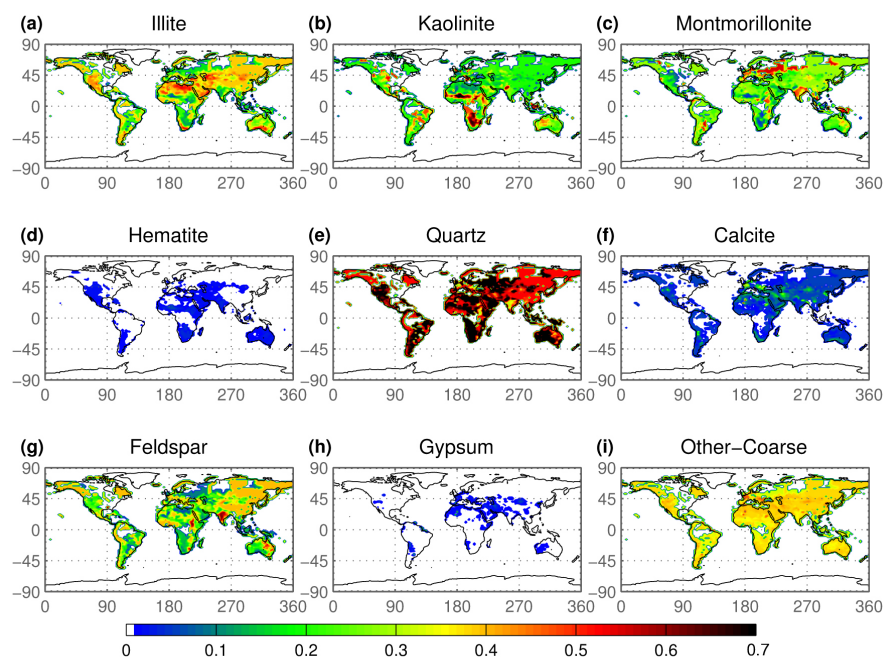
Figure 16: Model Single Scattering Albedo for CAM4 with tuned dust (a), CAM5 with tuned dust (b), CAM4 with mineralogy (c), and CAM5 with mineralogy (d).

Figure S1. Spatial distribution of annual all-sky radiative forcing (SW+LW) at the top of atmosphere for CAM4 with tuned dust and with tuned dust + release size (a,c) and for CAM5 with tuned dust and tuned dust+release size (b,d).

Figure S2. Spatial distribution of annual all-sky radiative forcing (SW+LW) at the top of atmosphere for CAM4 with tuned dust and with mineralogy + hematite in soil clay only (a,c) and for CAM5 with tuned dust and mineralogy + hematite in soil clay only (b,d).

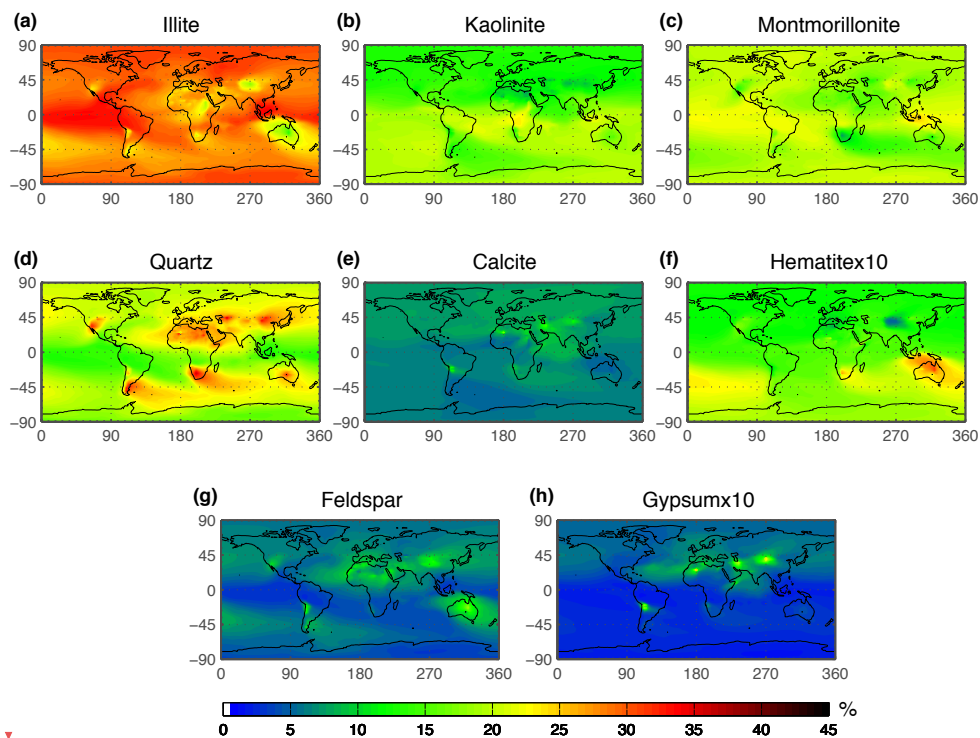
ras486 11/17/14 3:13 PM
Deleted: 15

1386
1387
1388
1389
1390
1391
1392



1393

ras486 11/17/14 3:13 PM
Deleted: Figure 1
ras486 11/17/14 3:13 PM
Deleted: Figure 2

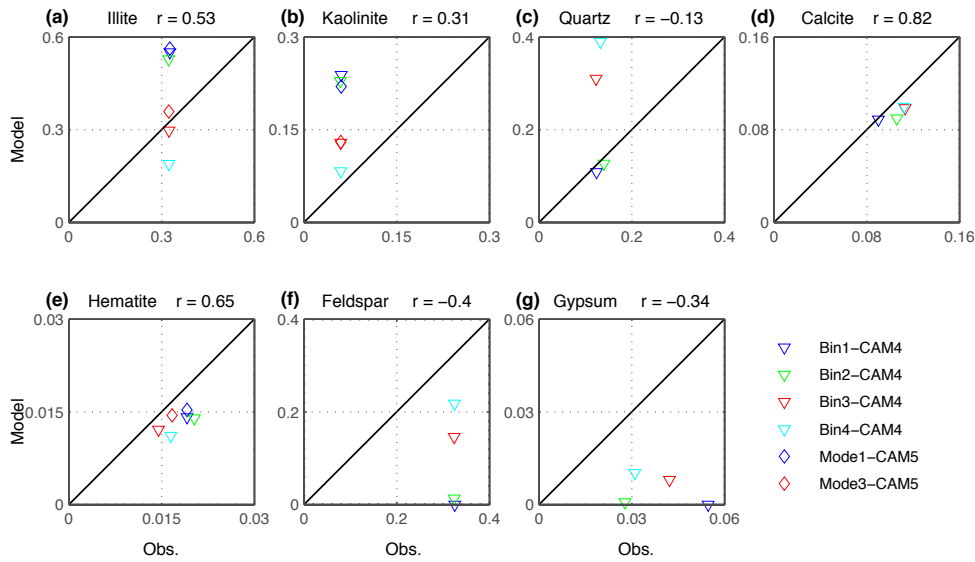
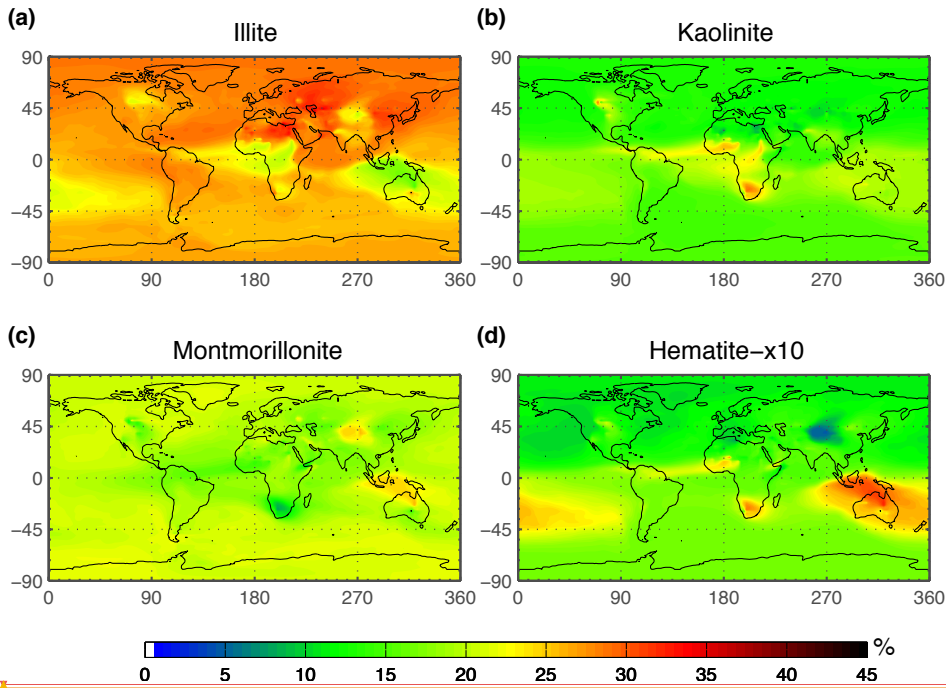


ras486 11/17/14 3:13 PM

Deleted: Figure 2

ras486 11/17/14 3:13 PM

Deleted: Figure 3



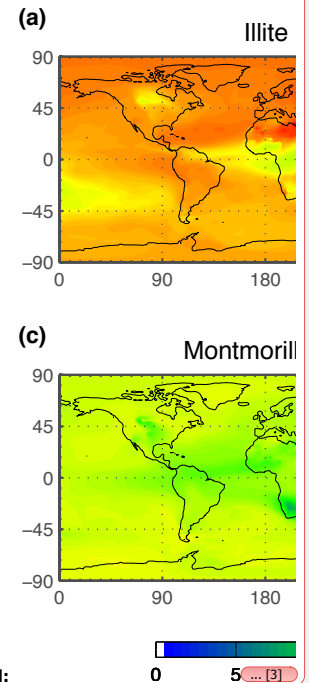
ras486 11/17/14 3:13 PM

Deleted: Figure 3

Unknown

Formatted: Font: +Theme Headings, Bold

ras486 11/17/14 3:13 PM



Deleted:

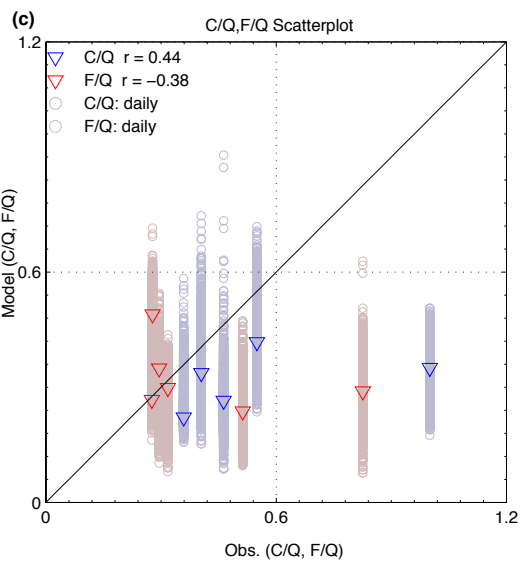
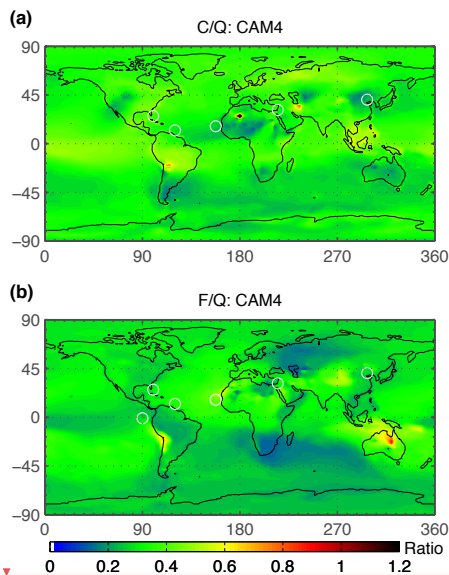
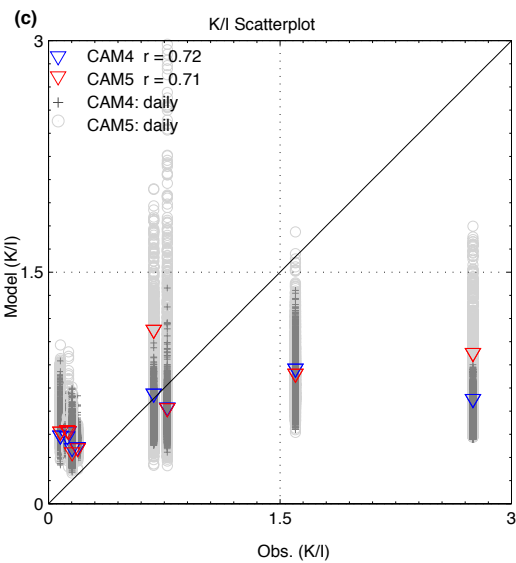
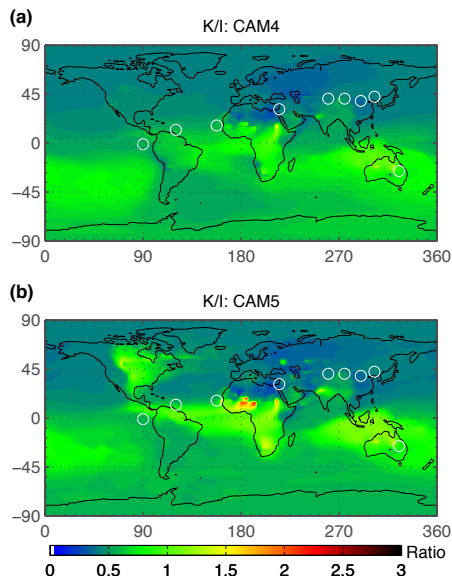
Unknown

Formatted: Font: +Theme Headings, Bold

ras486 11/17/14 3:13 PM

Deleted:

... [4]



ras486 11/17/14 3:13 PM

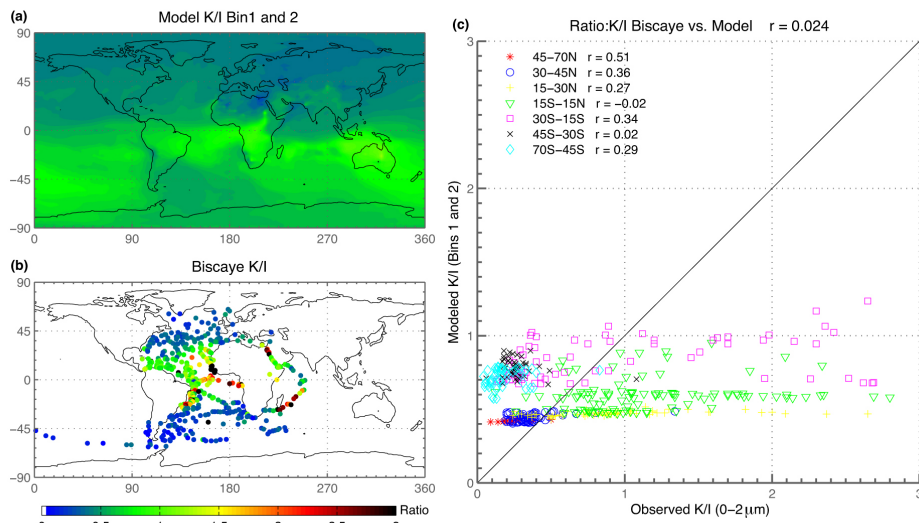
Deleted: .

... [5]

ras486 11/17/14 3:13 PM

Deleted: .

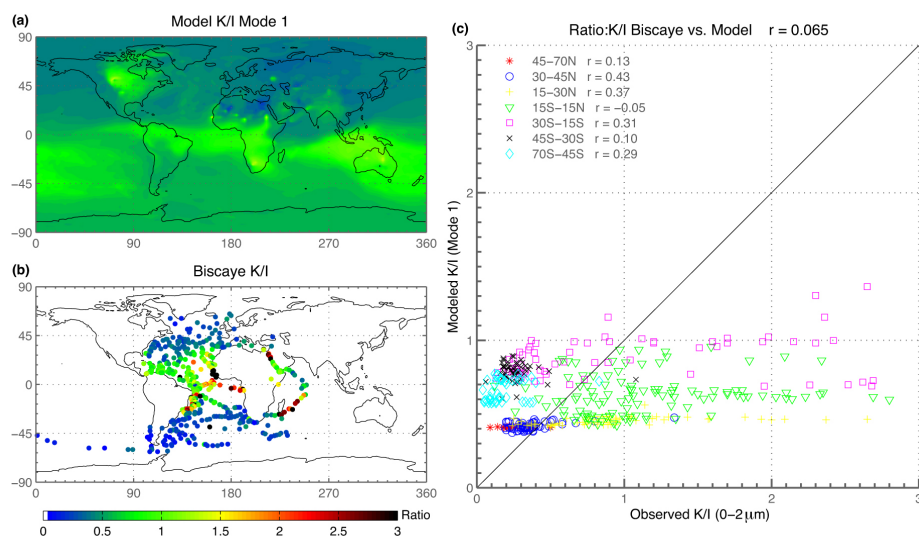
... [6]



ras486 11/17/14 3:13 PM

Deleted: -

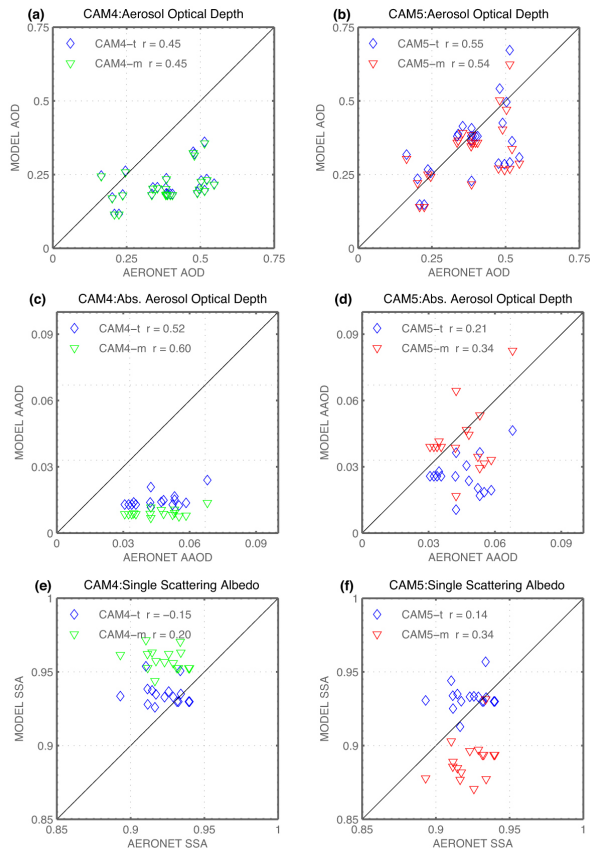
[7]



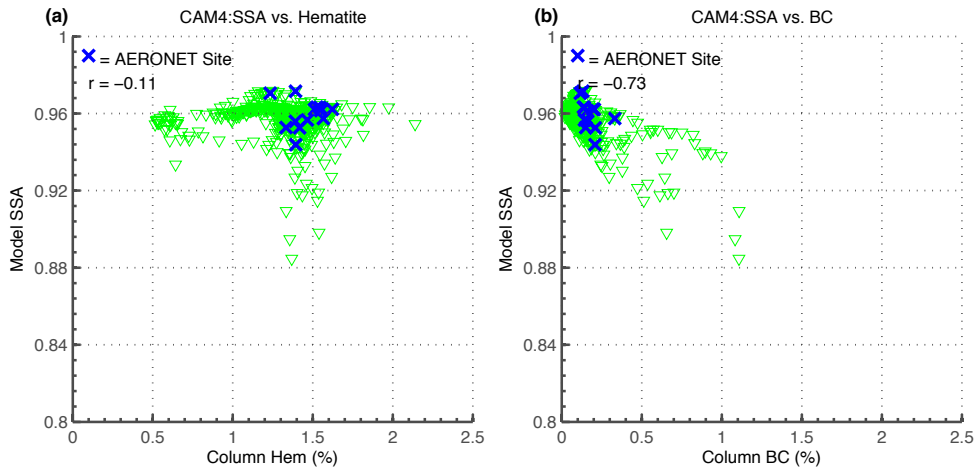
ras486 11/17/14 3:13 PM

Deleted: -

[8]



1436



1437
1438

ras486 11/17/14 3:13 PM

Deleted: .

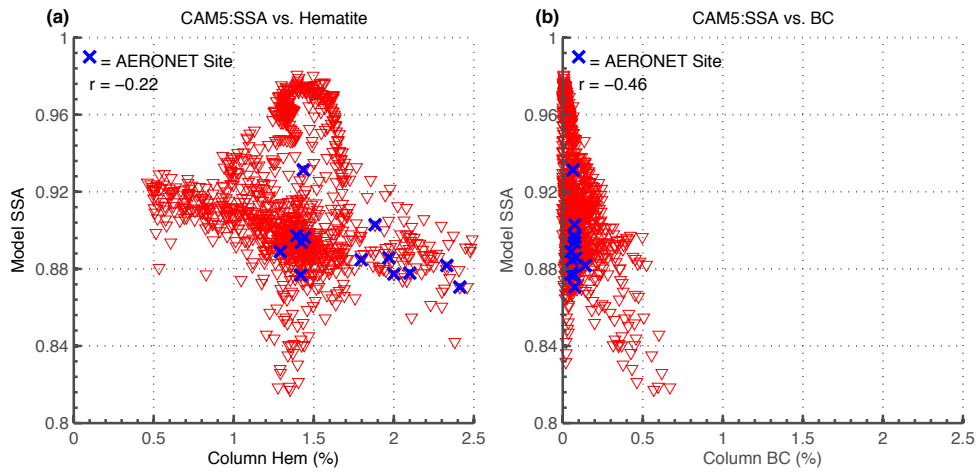
[9]

ras486 11/17/14 3:13 PM

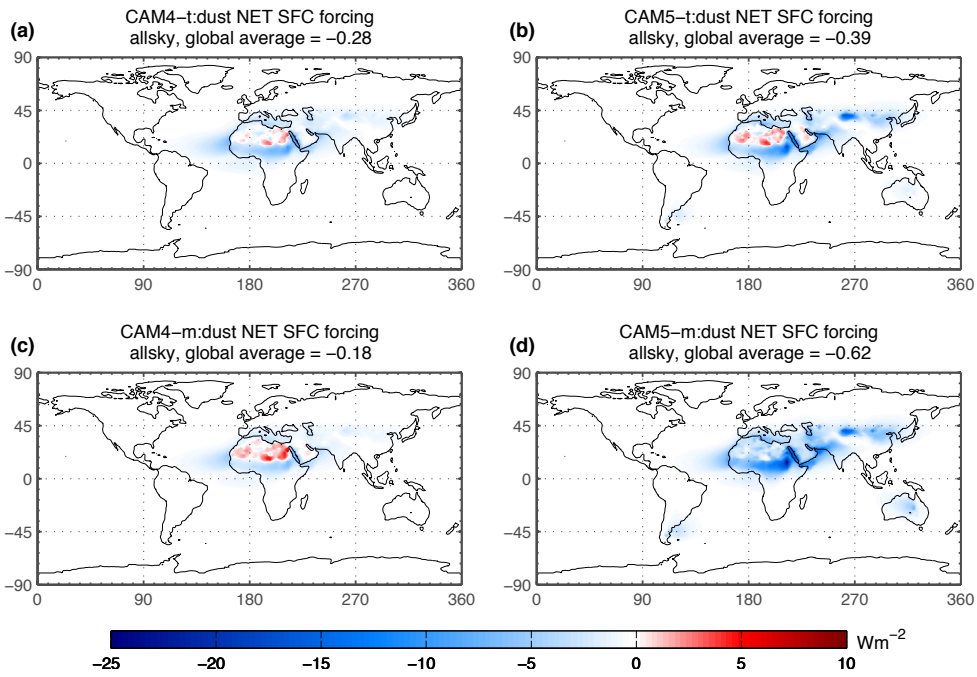
Deleted: .

[10]

1445



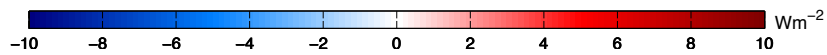
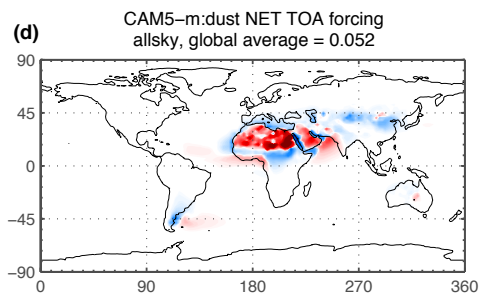
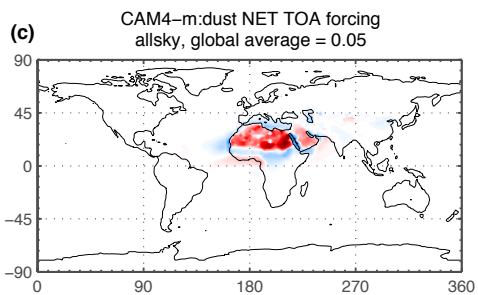
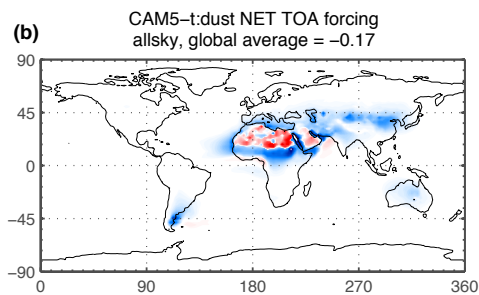
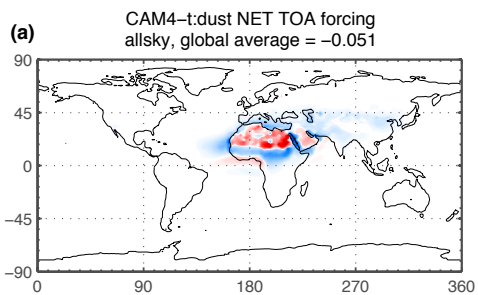
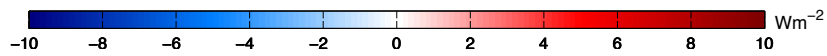
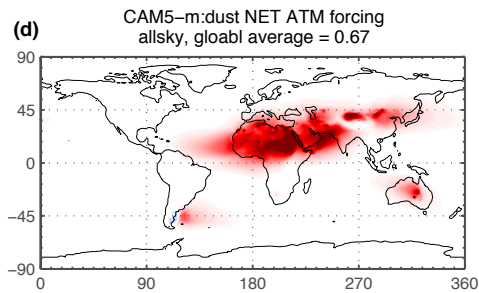
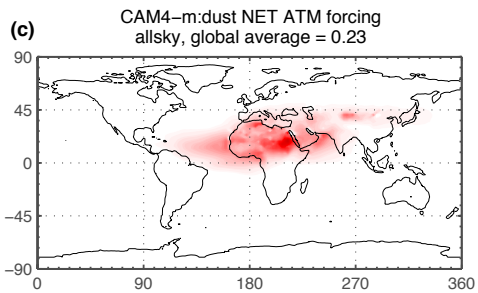
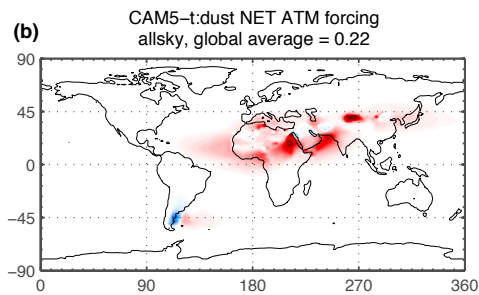
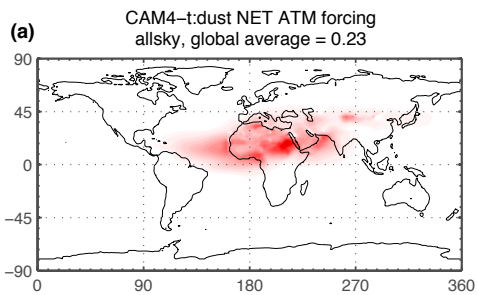
1446



1451

ras486 11/17/14 3:13 PM
Deleted: ... [11]

ras486 11/17/14 3:13 PM
Deleted: ... [12]



ras486 11/17/14 3:13 PM

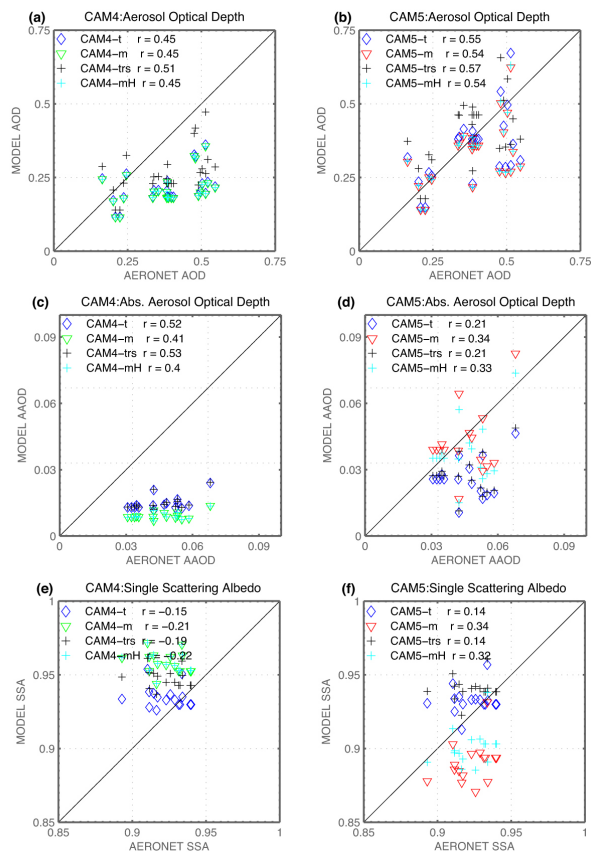
Deleted: .

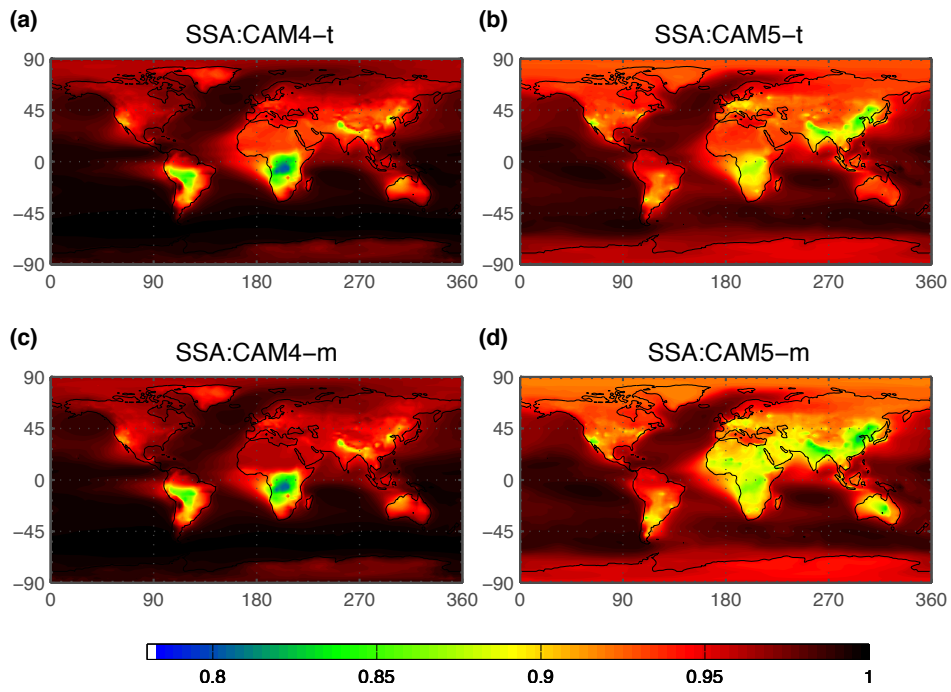
... [13]

ras486 11/17/14 3:13 PM

Deleted: .

... [14]





1472